

AD-A166 279

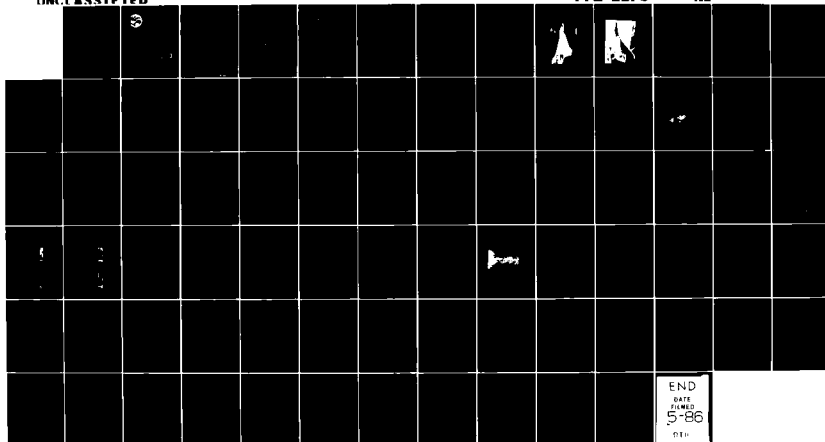
PRELIMINARY RESEARCH ON POST-STALL AERODYNAMICS(U)
POSEIDON RESEARCH IRVINE CA S C CROW ET AL. SEP 85
TR-81 AFOSR-TR-86-0073 F49620-84-C-0084

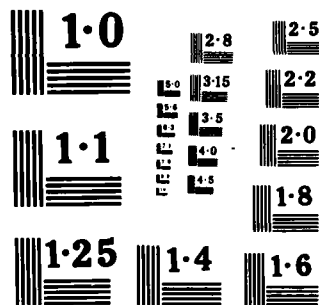
1/1

UNCLASSIFIED

F/G 20/4

NL





AD-A166 279

AFOSR-TR. 86-0073

(2)



Report No. 81

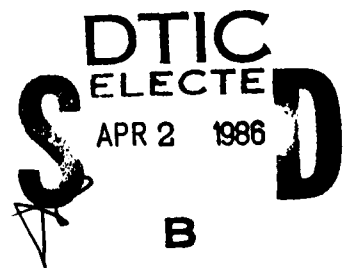
POSEIDON RESEARCH

Preliminary Research On Post-Stall Aerodynamics

S. C. Crow
R. B. Myers

September 1985

Prepared for the
Air Force Office
of
Scientific Research



DTIC FILE COPY

18 Mason • Irvine • California • 92718

Approved for public release;
distribution unlimited.

86 4 1 093

UNCLASSIFIED

SECURITY CLASSIFICATION OF THIS PAGE (When Data Entered)

REPORT DOCUMENTATION PAGE		READ INSTRUCTIONS BEFORE COMPLETING FORM
1. REPORT NUMBER AFOSR-TR- 86-0073	2. GOVT ACCESSION NO.	3. RECIPIENT'S CATALOG NUMBER
4. TITLE (and Subtitle) Preliminary Research on Post-Stall Aerodynamics		5. TYPE OF REPORT & PERIOD COVERED Annual Technical Report August, 1985 - August 1986
7. AUTHOR(s) S. C. Crow and R. B. Myers		6. PERFORMING ORG. REPORT NUMBER Report No. 81
9. PERFORMING ORGANIZATION NAME AND ADDRESS Poseidon Research 18 Mason Irvine, CA 92718		8. CONTRACT OR GRANT NUMBER(s) F49620-84-C-0084
11. CONTROLLING OFFICE NAME AND ADDRESS <i>same as #14</i>		10. PROGRAM ELEMENT, PROJECT, TASK AREA & WORK UNIT NUMBERS <i>61102F 2307 /A1</i>
14. MONITORING AGENCY NAME & ADDRESS (if different from Controlling Office) Air Force Office of Scientific Research Bolling AFB, D. C. 20332		12. REPORT DATE September 1985
		13. NUMBER OF PAGES 73 + iii
		15. SECURITY CLASS. (of this report) UNCLASSIFIED
		15a. DECLASSIFICATION DOWNGRADING SCHEDULE
16. DISTRIBUTION STATEMENT (of this Report) Approved for public release; distribution unlimited.		
17. DISTRIBUTION STATEMENT (of the abstract entered in Block 20, if different from Report) Approved for public release; distribution unlimited.		
18. SUPPLEMENTARY NOTES None		
19. KEY WORDS (Continue on reverse side if necessary and identify by block number) Post-Stall Maneuverability, Separated Flow, Unsteady Aerodynamics, Vortex Shedding		
20. ABSTRACT (Continue on reverse side if necessary and identify by block number) Fundamental results for two and three dimensional unsteady flows are derived. A model for vortex shedding at salient edges is advanced. A two dimensional Euler solver that implements this vortex shedding mechanism is described. Results of applying this model to impulsively started flat plates with fixed and with oscillating chord at angle of attack are presented. Implications for manipulation of the vortex wake in a post stall maneuver are discussed. Extension of the numerical methodology to three dimensions is also discussed. Key words:		

UNCLASSIFIED

Acknowledgement

Research sponsored by the Air Force Office of Scientific Research (AFSC), under Contract F49620-84-C-0084. The United States Government is authorized to reproduce and distribute reprints for governmental purposes notwithstanding any copyright notation hereon.

DTIC
ELECTE
APR 2 1986
B

[illegible]

AIR FORCE SCHOOL OF SCIENTIFIC RESEARCH (AFSC)
 NOTICE OF RELEASE: SENT TO DTIC
 This technical report has been reviewed and is
 approved for public release IAW AFR 190-12.
 Distribution is unlimited.
 MATTHEW J. KEEFER
 Chief, Technical Information Division



Report No. 81

Preliminary Research On Post-Stall Aerodynamics

**S. C. Crow
R. B. Myers**

September 1985

**Prepared for the
Air Force Office
of
Scientific Research**

Contents

	<u>Page</u>
1. Introduction to Post-Stall Aerodynamics.....	1
2. Theoretical Foundations.....	7
a. Theorems.....	7
b. Applications in Two Dimensions.....	12
c. Vortex Shedding.....	19
3. Numerical Methods for Two-Dimensional, Unsteady, Separated Flow.....	25
a. Introduction.....	25
b. Advection of Free Vorticity.....	26
c. Representation of Wing Sections by Bound Vorticity.....	28
d. Conversion of Bound Vorticity into Free Vorticity.....	30
4. Computational Results for Two-Dimensional, Unsteady, Separated Flow.....	32
a. Impulsively Started Flat Plate at 90 Degrees Angle of Attack.....	32
b. Impulsively Started Flat Plate at 45 Degrees Angle of Attack.....	41
c. Impulsively Started Flat Plate with Oscillating Cross Section at 90 Degrees Angle of Attack.....	47
d. Conclusions from Two-Dimensional Simulations.....	51
5. Directions for Further Work in Two Dimensions.....	53
a. Code Modificatons Aimed at Economics.....	53
b. Calculations Aimed at Further Understanding of the Computational Model.....	53
c. Calculations Aimed at further Understanding of the Physics and of the Model.....	54

Poseidon Research Report No. 81

6. Numerical Methods for Three-Dimensional Unsteady Flow..... 55

References..... 58

Appendix A. Derivations of Force and Moment Theorems

Appendix B. Bound Vorticity on a Flat Plate

1. Introduction to Post-Stall Aerodynamics

Fighter aircraft have evolved for decades toward high speeds and high wing loadings. Advances in air-to-air weapons are bringing that line of evolution to a halt, and the advantage is passing to fighter with lower wing loadings and great agility. The new design direction is apparent in the F-16XL shown in figure 1.1. The Rockwell model in figure 1.2 displays further concessions to maneuverability.

Herbst (1980) has introduced the concept of "supermaneuverability" to characterize the design of future fighters. Supermaneuverability has two aspects: decoupling of orientation from flight path to allow the aircraft to function as a rotating gun platform, and flight at angles of attack far beyond the limits of stall.

Herbst uses simulated fighter engagements to assess the merits of post-stall (PST) maneuvers. Figure 1.3 shows time histories of speed V and angle of attack α for a PST fighter engaging a normal adversary. The engagement begins with the fighters approaching each other at a closing speed of 200 m/sec. The PST fighter executes a 180° turn at an of 90°, broadside to his flight path. His engine thrust balances centrifugal force as his flight speed drops to 20 m/sec. Realigning his thrust with his new flight path, he accelerates up the flight path of his hapless adversary.

Flight at such large angles introduces phenomena outside the boundaries of traditional aerodynamics. Some of those phenomena are evident in figure 1.4:

- Flow separates all around the planform edges. This produces the bag-shaped vortex sheet shown in cross section in figure 1.4.

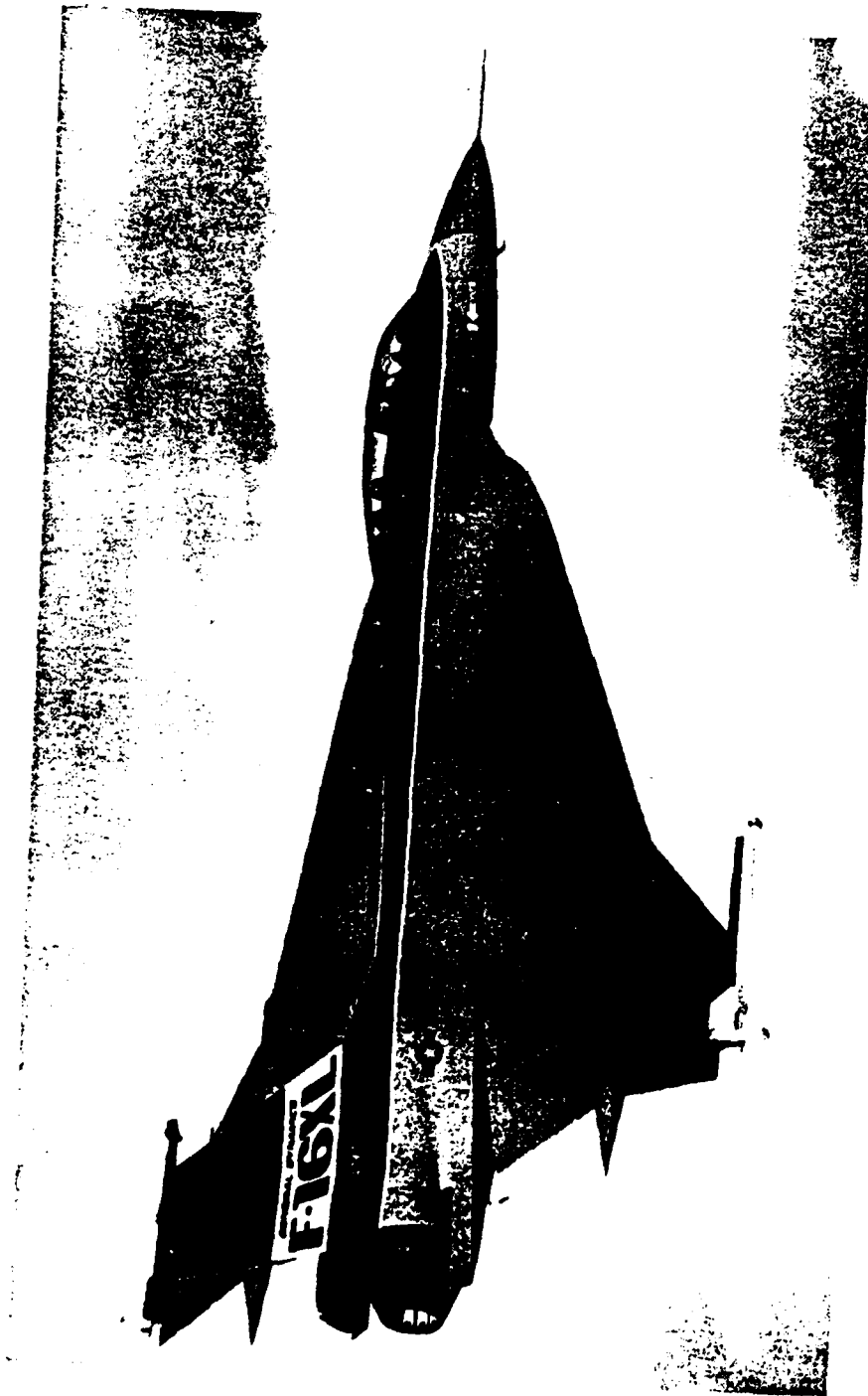


Figure 1.1. The F-16XL demonstrator aircraft. From the cover of Aviation Week & Space Technology, 13 December 1982.

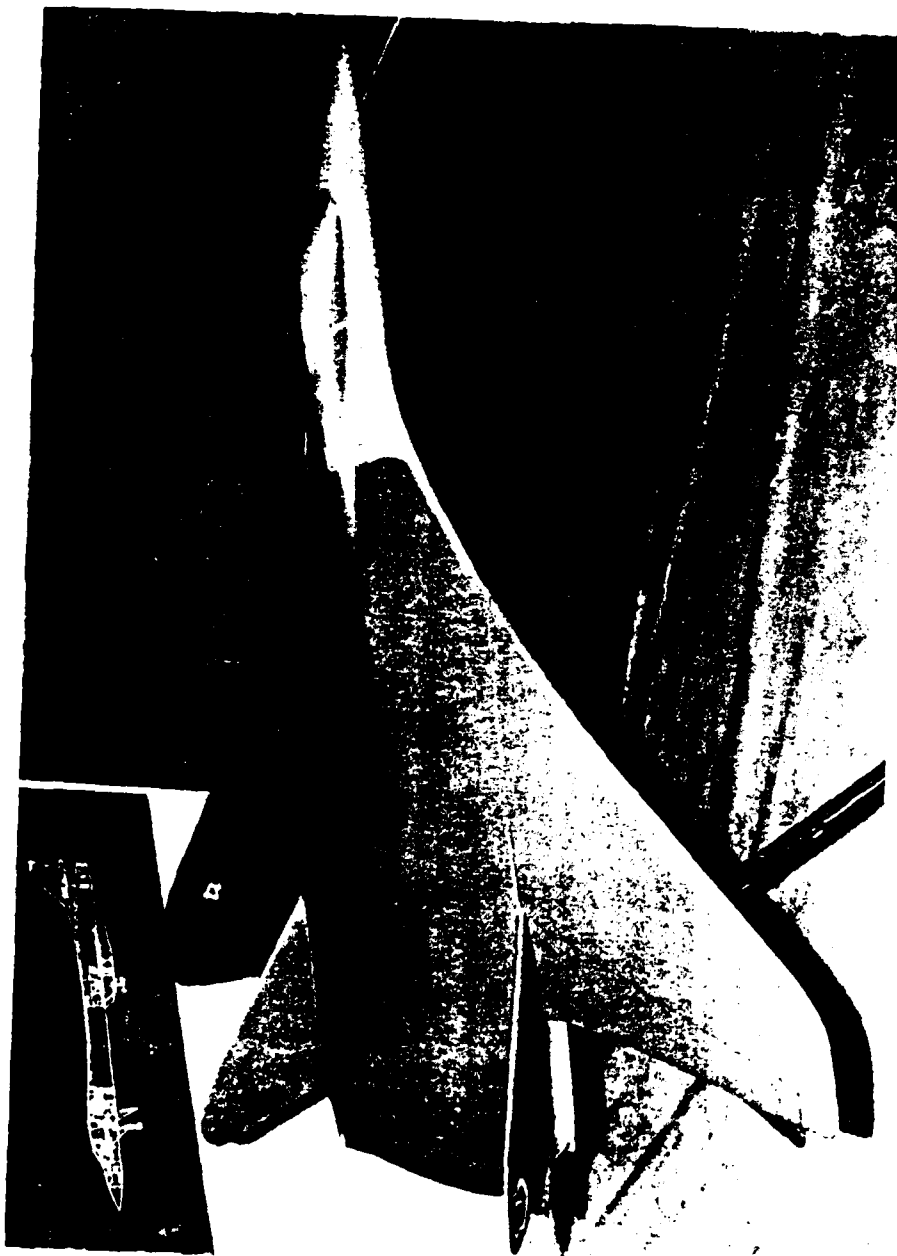


Figure 1.2. Rockwell model of an advanced tactical fighter. From page 45 of Aviation Week & Space Technology, 30 May 1983.

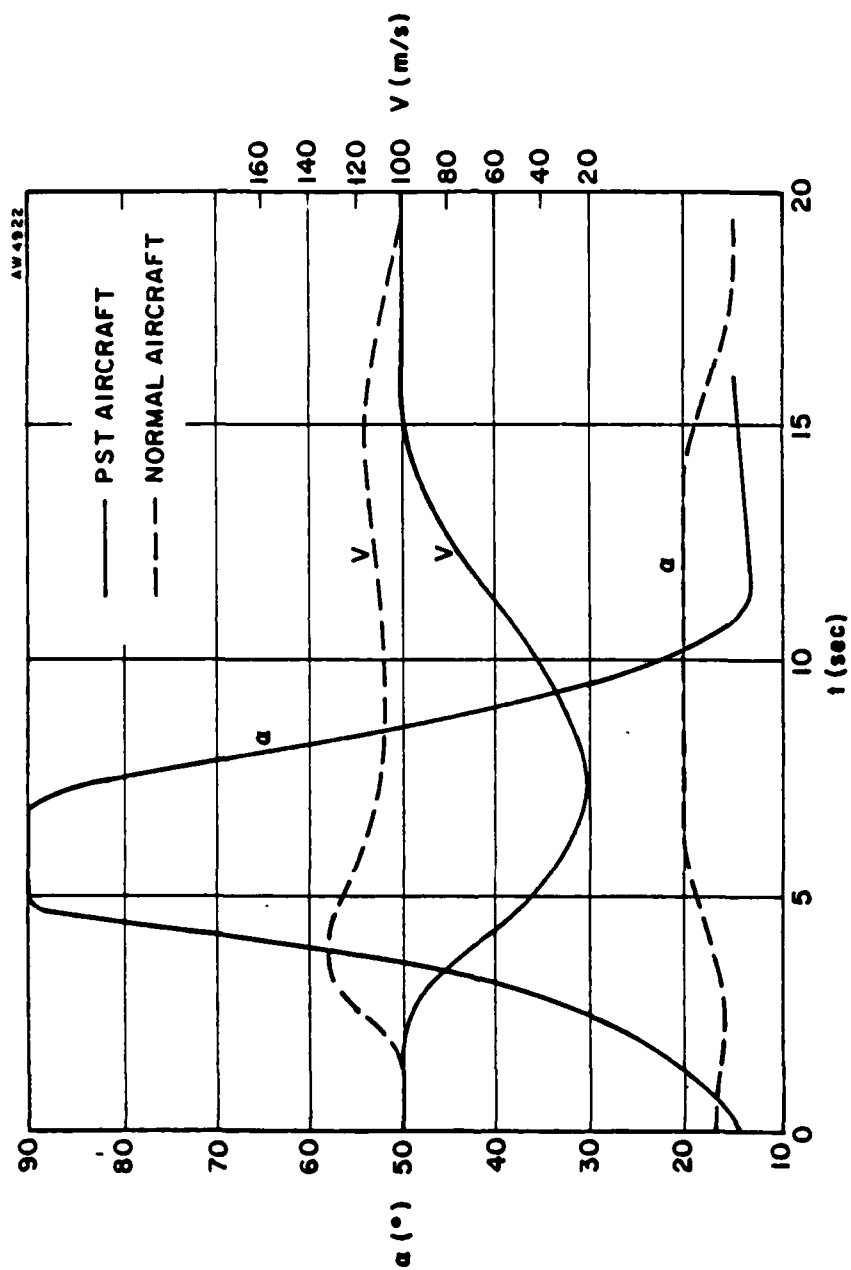


Figure 1.3. History of speed and angle of attack during a simulated engagement between a normal and a PST fighter. From Herbst (1980).

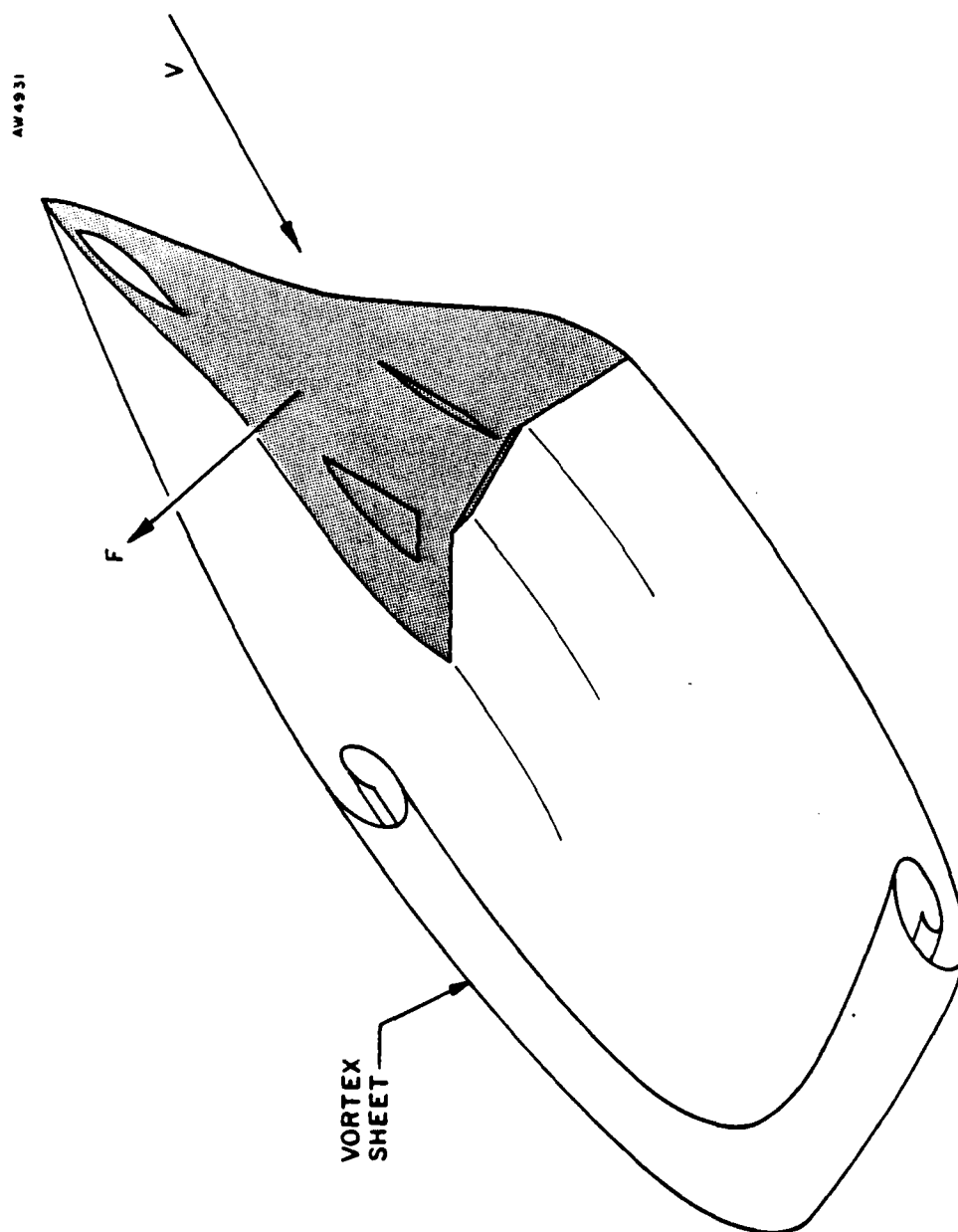


Figure 1.4. Bag-shaped vortex sheet formed by post-stall maneuver.

Poseidon Research Report No. 81

- Viscous effects are unimportant; a consequence of the violent and unambiguous separation on all salient edges of the planform.
- Pressure force is normal to the planform owing to a complete loss of leading-edge suction.
- The vortex sheet shed from the aircraft is strong, with a velocity jump comparable to the speed V of the aircraft.
- Shed vorticity interacts strongly with the aircraft, probably creating "vortex lift" like vorticity shed from leading edges of delta wings.
- The vorticity around the aircraft is nonsteady. Kelvin-Helmholtz instability of the vortex sheet precludes the attainment of a steady Helmholtz (free-streamline) flow, with dead air inside.

The phenomena above are beyond the reach of aerodynamic theories predicated upon quasi-steady flow or small perturbations. Numerical methods, as described here, almost certainly are required to handle the nonsteady, nonlinear vortex flow surrounding a PST aircraft and to predict the resulting aerodynamic forces.

2. Theoretical Foundations

a. Theorems

Our study of post-stall aerodynamics begins with the Euler equations for inviscid incompressible flow:

$$\rho \left(\frac{\partial \underline{u}}{\partial t} + \underline{u} \cdot \nabla \underline{u} \right) + \nabla p = \underline{f} , \quad (2.1)$$

$$\nabla \cdot \underline{u} = 0 . \quad (2.2)$$

In these equations ρ is density, p is pressure, \underline{u} is velocity, and \underline{f} is a force per unit volume exerted on the fluid by some external agency. The continuity equation (2.2) presumes that ρ is constant, an adequate approximation for low-speed maneuvers though not for transonic flight. The assumption of inviscid flow is warranted only if we can devise side conditions that accurately represent the conversion of boundary-layer vorticity into free vorticity at planform edges, a matter discussed in part (c) of this chapter.

Equations (2.1) and (2.2) apply to fluid outside the aircraft surface, on which normal velocity boundary conditions are imposed. Conceptually and computationally, it is often convenient to regard the fluid as filling all space, with (2.1) and (2.2) applying everywhere, and with the aircraft surface represented by some distribution of singularities, sources and bound vortex sheets being popular choices. Completely equivalent to a vortex sheet is a dipole sheet, which is a volumetric force concentrated on the surface of the body and distributed over the surface so as to enforce the normal velocity boundary condition. Such a representation is achieved by writing \underline{f} as

$$\underline{f} = \Delta p \delta(n) \hat{n} , \quad (2.3)$$

where Δp is the pressure jump across the dipole sheet, $\delta(n)$ is a delta function of the normal coordinate n , and \hat{n} is the unit outward normal vector. The pressure jump Δp is a function of time and of two surface coordinates and is tailored to insure that

$$\underline{u} \cdot \hat{n} = v_n , \quad (2.4)$$

where v_n is the local normal component of boundary velocity. With this representation, equations (2.1) and (2.2) apply throughout a hypothetical unbounded fluid pervading the aircraft body.

Recall that \underline{f} is a volumetric force exerted by an external agency (the aircraft) on the fluid. the net force exerted by the fluid on the aircraft is therefore given by the volume integral

$$\underline{F} = - \int_V \underline{f} \, dV , \quad (2.5)$$

where the region of integration V extends over all space. A similar formula provides the net moment exerted by the fluid on the aircraft:

$$\underline{M} = - \int_V \underline{x} \times \underline{f} \, dV . \quad (2.6)$$

The dipole representation (2.3) allows an immediate evaluation of \underline{F} and \underline{M} without a need for computing pressure.

There is no simple integral relation between \underline{F} or \underline{M} and \underline{u} , because \underline{u} does not fall toward zero fast enough to permit a proper evaluation of integrals like

$$\int_V \underline{u} \, dV .$$

There are, however, simple relations of \underline{F} and \underline{M} to vorticity $\underline{\omega}$, the curl of the velocity field:

$$\underline{\omega} = \nabla \times \underline{u} . \quad (2.7)$$

Vorticity $\underline{\omega}$ is a complete flow representation when \underline{u} is divergence free. Velocity may then be written as the curl of a vector potential ,

$$\underline{u} = \nabla \times \underline{\psi} , \quad (2.8)$$

with

$$\nabla^2 \underline{\psi} = - \underline{\omega} . \quad (2.9)$$

Given $\underline{\omega}$, one solves the Poisson equation (2.9) for $\underline{\psi}$, from which \underline{u} follows by (2.8). Of course $\underline{\omega}$ includes both actual "free" vorticity $\underline{\omega}_f$ in the fluid, and "bound" vorticity $\underline{\omega}_b$ associated with the dipole sheet representing the body:

$$\underline{\omega} = \underline{\omega}_b + \underline{\omega}_f . \quad (2.10)$$

$\underline{\omega}_b$ is the concentrated vortex sheet that would appear in a vortex-panel code.

Vorticity evolves according to an equation obtained by taking the curl of (2.1):

$$\frac{\partial \underline{\omega}}{\partial t} + \underline{u} \cdot \nabla \underline{\omega} - \underline{\omega} \cdot \nabla \underline{u} = \nabla \times \underline{g} \quad (2.11)$$

where

$$\underline{g} = \underline{f}/\rho . \quad (2.12)$$

We can derive a relation between \underline{F} and $\underline{x} \times \underline{\omega}$ by taking the cross-product of \underline{x} with (2.11) and integrating over all space, using the facts that $\underline{\omega}$ and \underline{g} are zero outside some finite region. The net moment \underline{M} bears a corresponding relation with $\underline{x} \times \underline{x} \times \underline{\omega}$. Appendix A shows how the integral relationships are derived.

The force and moment theorems must be derived separately for two and three-dimensional flows, because a two-dimensional vorticity field is unbounded in the third dimension, which changes the convergence properties of integrals. A two-dimensional field of vorticity aligned with the z-axis has the form

$$\underline{\omega} = \omega(x, y, t) \hat{e}_z . \quad (2.13)$$

Net force per unit length in the z-direction has the form

$$\underline{F} = - \rho \frac{d}{dt} \int_A \underline{x} \times (\omega \hat{e}_z) dA , \quad (2.14)$$

where the integration extends over the full (x, y) plane, or at least over every part containing non-zero vorticity. Moment per unit length has the form

$$\underline{M} = \frac{\rho}{2} \frac{d}{dt} \int_A (x^2 + y^2) (\omega \hat{e}_z) dA , \quad (2.15)$$

directed along the z-axis. Those are reactions exerted on the aircraft by the fluid.

The corresponding results in three dimensions are as follows:

$$\underline{\underline{F}} = - \frac{\rho}{2} \frac{d}{dt} \int_V \underline{\underline{x}} \times \underline{\underline{\omega}} dV ; \quad (2.16)$$

$$\underline{\underline{M}} = - \frac{\rho}{3} \frac{d}{dt} \int_V \underline{\underline{x}} \times (\underline{\underline{x}} \times \underline{\underline{\omega}}) dV . \quad (2.17)$$

Equations (2.14), (2.15) or (2.16), (2.17) allow us to evaluate forces and moments from vorticity without the intervention of pressure.

b. Applications in Two Dimensions

Figure 2.1 shows a typical situation where we might want to apply the theorems of part (a) in two dimensions. A thin airfoil starts from rest, shedding vorticity from its trailing edge and possibly from its leading edge. The airfoil can be represented as a sheet of bound vorticity,

$$\omega_b(x, y, t) = \gamma(s, t) \delta(n) , \quad (2.18)$$

where s and n are coordinates parallel and normal to the airfoil respectively, $\delta(n)$ is the delta function expressing the concentration of the bound vortex sheet, and $\gamma(s, t)$ is the velocity jump from the bottom to the top of the airfoil:

$$\gamma = u_2 - u_1 . \quad (2.19)$$

According to the Kelvin circulation theorem, the net vorticity over the entire plane remains zero for all time if the flow starts from rest:

$$\Gamma = \int_A (\omega_b + \omega_f) dA = 0 . \quad (2.20)$$

Equation (2.20) is an important constraint on the assignment of bound vorticity to represent the airfoil. The drag and lift on the airfoil follow from (2.14):

$$D = -\rho \frac{d}{dt} \int_A y(\omega_b + \omega_f) dA , \quad (2.21)$$

$$L = \rho \frac{d}{dt} \int_A x(\omega_b + \omega_f) dA . \quad (2.22)$$

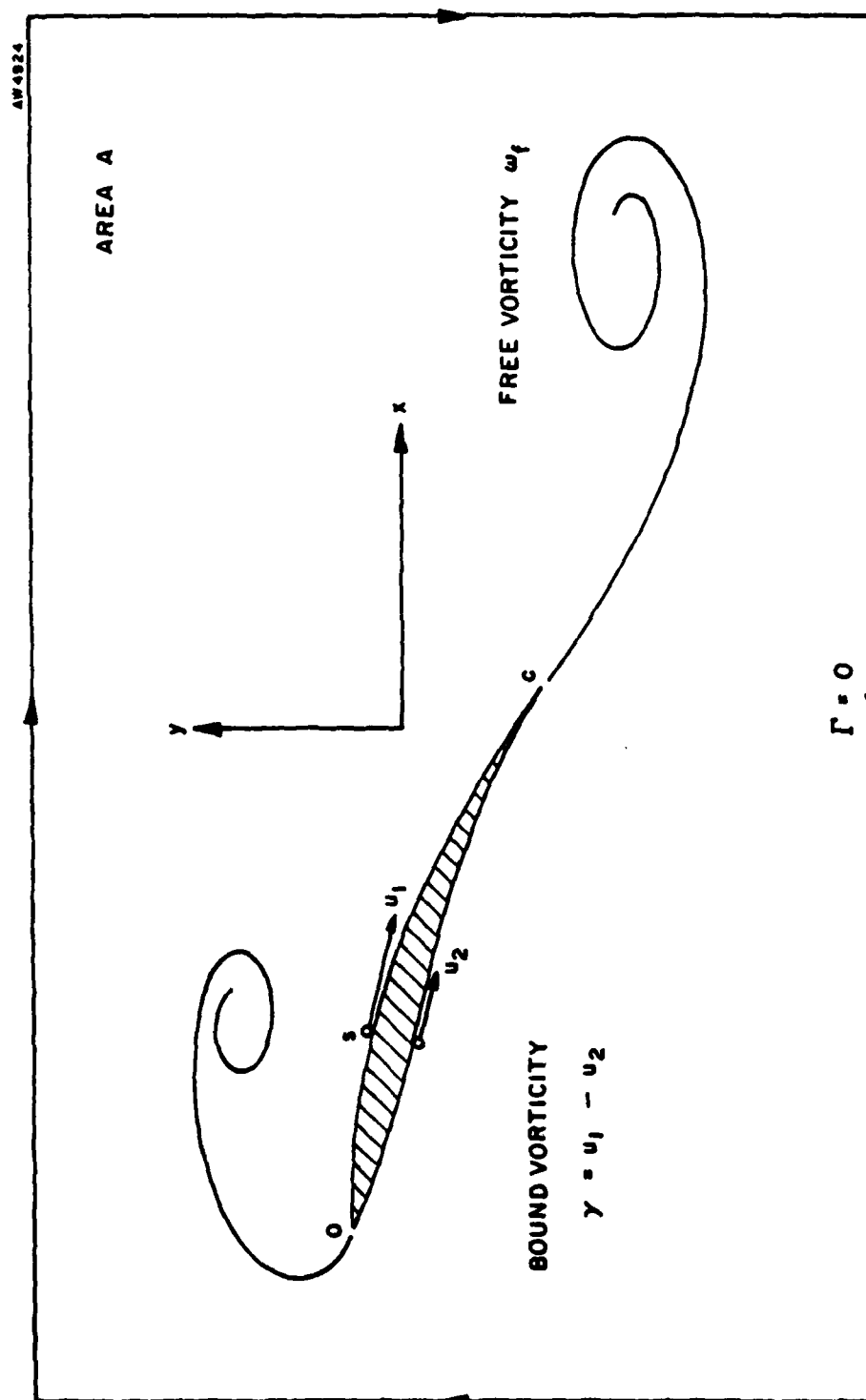


Figure 2.1. Bound and free vorticity in two dimensions.

If the airfoil eventually stops shedding vorticity, then the free vorticity ω_f wraps into a starting vortex with constant circulation and a centroid fixed in space, i.e.

$$\frac{d}{dt} \int_A \underline{x} \omega_f dA \rightarrow 0 . \quad (2.23)$$

The bound vorticity becomes steady in coordinates $(X = x + Vt, y)$ moving leftward with the airfoil at its velocity V . Thus

$$D \rightarrow -\rho \frac{d}{dt} \iint y \omega_b(X, y) dXdy = 0, \quad (2.24)$$

and

$$\begin{aligned} L &\rightarrow \rho \frac{d}{dt} \iint (X - Vt) \omega_b(X, y) dXdy \\ &\rightarrow -\rho V \int_A \omega_b dA = \rho V \Gamma_b , \end{aligned} \quad (2.25)$$

where Γ_b is the circulation around the airfoil defined in the clockwise sense familiar in aerodynamics. Equation (2.15) is D'Alembert's paradox of zero drag in steady flow, and (2.16) is the Kutta-Joukowski theorem for lift. Those results should help build confidence in (2.14) as the general force law for non-steady two-dimensional flow.

A key assumption in our derivation of the Kutta-Joukowski theorem was that vortex shedding ceases after some time, so the flow becomes

steady in airfoil-fixed coordinates. Violation of that assumption is one of the defining characteristics of post-stall aerodynamics.

One way vortex shedding can continue indefinitely is for shedding to occur at both the leading and trailing edges of the airfoil. As long as vorticity shed from the leading edge has sign opposite that shed from the trailing edge, shedding can continue without violating the vorticity conservation theorem (2.20). As the two vortex sheets lengthen, they might even assume an appearance of steadiness in the vicinity of the airfoil.

Helmholtz developed the holograph method to study such flows around flat plates, as illustrated in figure 2.2(a) (Lamb 1932). Helmholtz derived the formula

$$F = \frac{\pi \sin \alpha}{4 + \pi \sin \alpha} \rho V^2 c \quad (2.26)$$

for force per unit length normal to an infinite flat plate (lamina) of chord c . We might have hoped that Helmholtz's solutions become asymptotically valid for post-stall flows at long times after pitch-up. Such hope is unwarranted, because the free shear layers of Helmholtz flows are subject to a Kelvin-Helmholtz instability as shown in figure 2.2(b). Steady-state free-streamline theory predicts a zero-velocity wake with a uniform pressure equal to the ambient pressure far upstream. Eddies resulting from the instability, however, scavenge the wake and lower the backpressure on the plate.

Equation (2.26) predicts a drag coefficient of 0.88 for a plate normal to the flow, whereas the measured value is 1.98 (Hoerner 1965). The 125 percent increase is attributable to nonsteady vortex suction, not too surprising in view of the origin of aerodynamic forces evident in (2.21) and (2.22).

AW4932

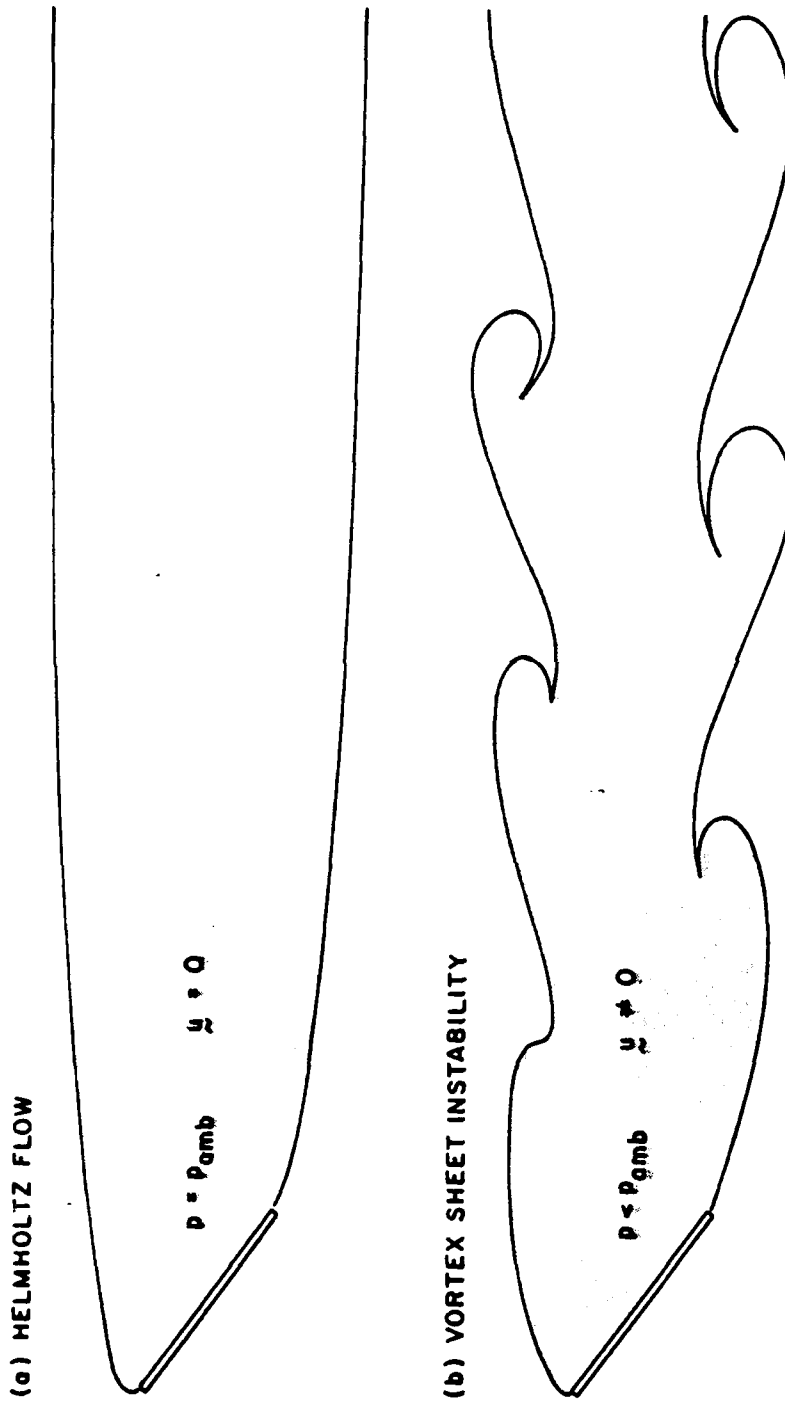


Figure 2.2. Helmholtz flow (a) and its nonsteady counterpart (b) likely to be seen in practice.

Vortex suction plays an important role in the lift of delta wings at large angles of attack. Indeed the flow around a delta wing is a prototype for post-stall aerodynamics. Figure 2.3 shows a delta wing inclined at a substantial angle α to the flow. A plane A traverse to the delta-wing planform moves with the fluid at speed V . The delta wing intersects the transverse plane as a slit of varying span $b(t)$, moving downward at a speed $V \sin \alpha$. Vorticity shed from the leading edge of the delta wing appears as free vorticity in the transverse plane. If the delta wing is slender, then the flow in the transverse plane can be treated like the two-dimensional time-dependent flow of figure 2.1. In particular, the lift per unit length along the delta wing is given by equation (2.22) evaluated in the fluid-fixed transverse plane.

There is no fully satisfactory theory for the vortex lift of delta wings. Vortex-lift calculations rely instead on analogies. Hoerner (1975) describes an end-plate analogy, whereby the leading-edge vortices are regarded as acting like end plates, increasing the effective span in the transverse plane. Polhamus (1971) achieved good correlation with data on the basis of a leading-edge suction analogy, where the leading-edge suction that reduces the drag of an attached flow is rotated 90° to produce lift normal to the planform. Neither analogy is convincing as a basis for a venture into post-stall aerodynamics.

A key difficulty with the concept of vortex lift is evident from equation (2.22): vortex lift arises from the time dependence of free vorticity in the two-dimensional flow of figure 2.1 or in the transverse plane of figure 2.3. Steady vortices in such situations exert no net force on bodies. A satisfactory method for predicting the vortex lift of delta wings should be among the first products of post-stall aerodynamics.

AW 4925

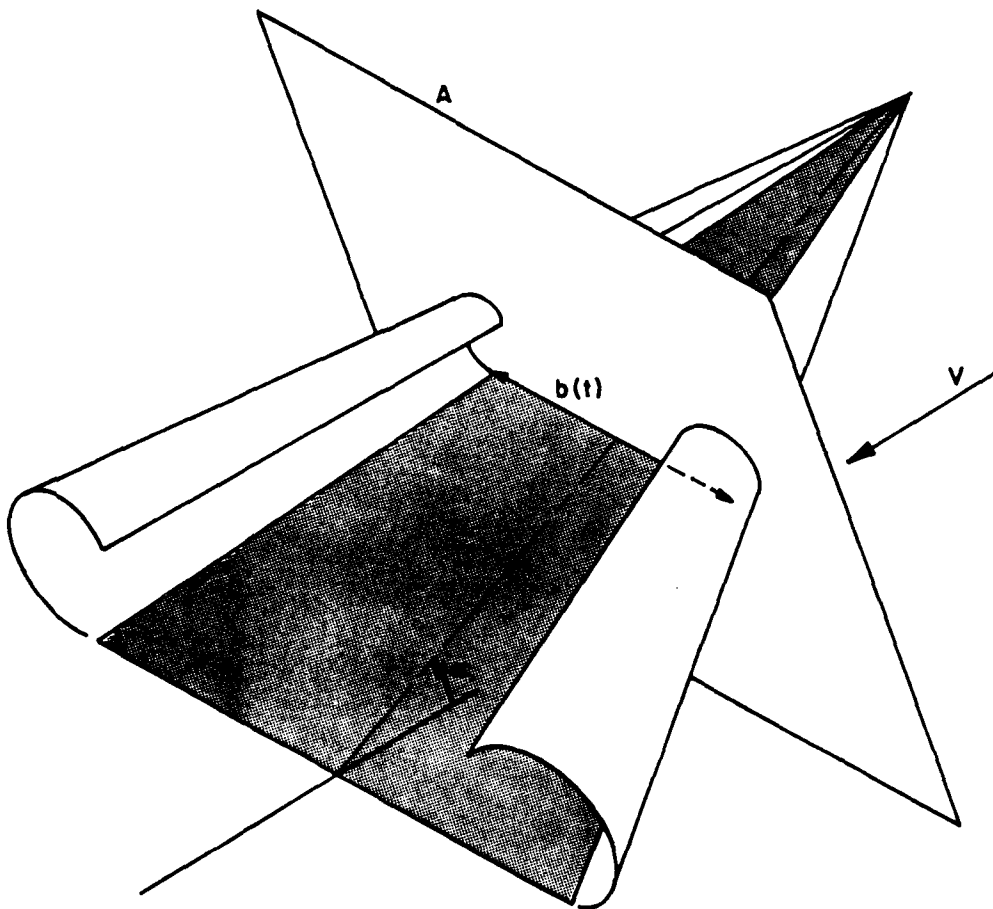


Figure 2.3. Transverse-plane interpretation of flow over a delta wing. The flow may be steady in wing-fixed coordinates but is nonsteady in the fluid-fixed transverse plane.

c. Vortex Shedding

We have assumed so far that the flow is inviscid, though it may contain "free" vorticity and "bound" vorticity representing the surfaces of bodies. The distinction between bound and free vorticity is peculiar to the assumption of inviscid flow and would disappear if we were willing to deal with viscous diffusion. "Bound" vorticity is simply vorticity in boundary layers, subject to viscous and inertial dynamics about equally. "Free" vorticity is vorticity that has escaped far enough from boundaries to be subject mainly to inertial rather than to viscous dynamics. The escape process is called vortex shedding, meaning the transformation of bound into free vorticity.

The reason for maintaining a distinction between bound and free vorticity is that we hope to analyze post-stall aerodynamics using inviscid flow equations. This hope, however, requires us to postulate a rule for transforming bound into free vorticity without explicit reliance on the Navier-Stokes equations of viscous flow. Such a rule is unlikely to become available for bodies of general shape, where both the location and rate of vortex shedding are variable. We therefore confine attention to salient edges, from which vorticity can be expected to shed almost all the time.

The search for inviscid shedding rules is a challenge for computational fluid dynamics. Some authors (e.g. Hitzel and Schmidt 1984) invoke compressibility as a shedding mechanism.* Compressibility will be of no help to us, because we want to study incompressible flows. It is far from clear, moreover, that compressible effects can mimic viscous flow separation.

*As did Rayleigh, interestingly, shortly before Prandtl's 1905 paper on the boundary-layer concept.

Another school of thought holds that finite difference schemes by their very nature adequately simulate the effects of viscosity with respect to vortex shedding at salient edges (Rizzi and Eriksson 1984). There is merit to this viewpoint if velocity is one of the advected quantities. Upwind differencing, in particular, seems almost certain to project velocity discontinuities (vortex sheets) from a sharp edge into the computational grid. We have based the two-dimensional computations presented here on the vorticity equation, however, which sustains zero vorticity as a solution unless free vorticity is injected deliberately into the finite-difference grid. We must provide an explicit algorithm for the creation of free vorticity.

Our vortex shedding algorithm is based on the fact mentioned above that bound vorticity is vorticity in boundary layers. A boundary layer cannot flow around a sharp edge but must separate from it if the direction of flow is from the material boundary toward free fluid. The rate of creation of free vorticity is the integrated flux of boundary-layer vorticity flowing across the edge.

Figure 2.4(a) illustrates the principles of vortex shedding in two dimensions when the flow is directed away from the body both above and below an edge. Consider the situation above the edge, and adopt local coordinates (x, y) such that x is parallel to the upper surface and y is normal to it. Vorticity can be written everywhere as

$$\omega = \partial v / \partial x - \partial u / \partial y \quad . \quad (2.27)$$

In the boundary layer, v is small and x -derivatives are small, so on both counts vorticity can be approximated as

$$\omega \approx - \partial u / \partial y \quad . \quad (2.28)$$

The net vorticity flux across the edge in the upper boundary layer is

$$\int_0^{\delta} (u-u_0) \omega \, dy \quad , \quad (2.29)$$

where δ is the depth of the boundary layer, and u_0 accounts for the possibility that the upper surface of the body is moving at a speed u_0 parallel to itself. Adopting the boundary-layer approximation (2.28) for ω and integrating through the boundary layer, we obtain

$$- \int_0^{\delta} (u-u_0) \frac{\partial u}{\partial y} \, dy = - \frac{(u_1-u_0)^2}{2} \quad (2.30)$$

as the expression for net vorticity flux consistent with thin boundary layers. Here u_1 is the value of u at the top of the boundary layer, i.e. the surface slip velocity of inviscid flow theory, while u_0 is the value of u at the boundary consistent with the actual no-slip boundary condition.

Though (2.30) is based on boundary-layer theory, the formula contains no explicit reference to viscosity. This supports the hope that post-stall aerodynamics can be treated by inviscid flow methods as long as the shedding rule correctly embodies the boundary-layer concept.

Similar reasoning about the underside of the surface leads to the total vorticity flux expressed in figure 2.4(a). Notice that

$$\begin{aligned} \frac{(u_2 - u_0)^2}{2} - \frac{(u_1 - u_0)^2}{2} &= \left(\frac{u_1 - u_2}{2} \right) - u_0 (u_2 - u_1) \quad (2.31) \\ &= (\bar{u} - u_0) \gamma \quad , \end{aligned}$$

AW4937

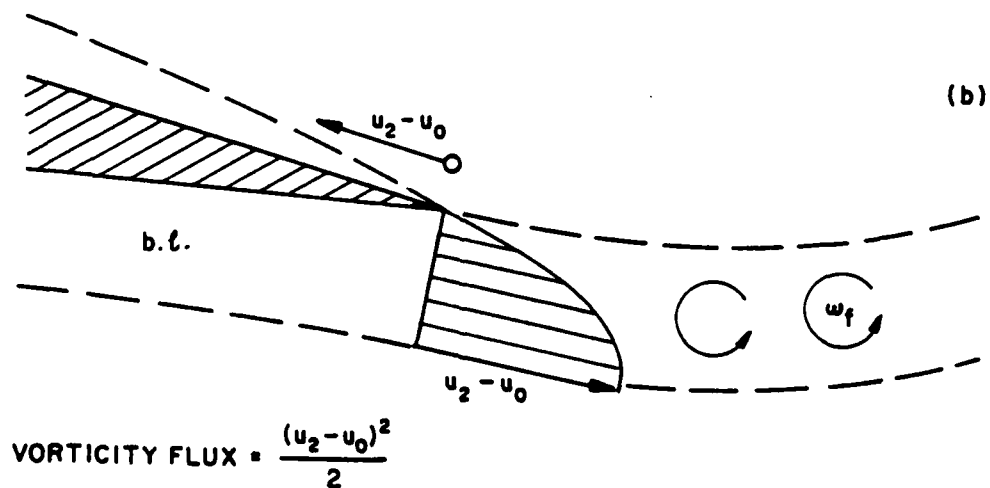
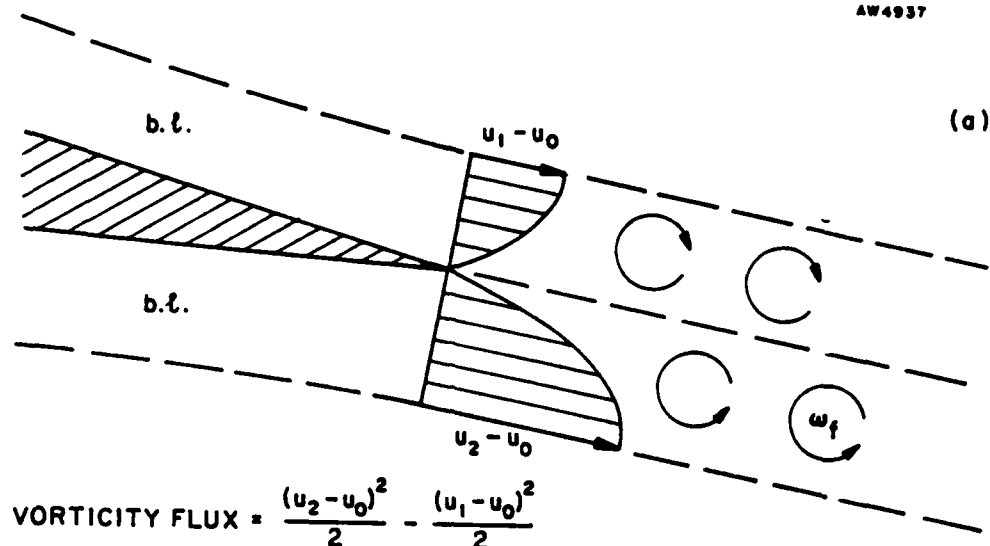


Figure 2.4. Transformation of bound into free vorticity.

i.e. the net vorticity flux equals the strength γ of the vortex sheet at the edge times the free-stream velocity relative to the edge averaged above and below the lifting surface.

The situation in figure 2.4(a) is not the only possibility. The free-stream velocity relative to the edge might be directed inward from the edge above the surface, below the surface, or both. Figure 2.4(b) illustrates the consequences of an inward-directed velocity above the surface. No boundary-layer vorticity sheds from the upper surface, and only the first term on the left of (2.31) contributes to a vorticity flux. The simple interpretation of vorticity transformation afforded by the right of (2.31) is lost, but the phenomenology is clear.

Our vortex shedding rule must specify not only how much free vorticity is created, but also where it is place in the computational grid. Figure 2.5 shows how the placement is effected in the code described in later sections. Free vorticity is injected into the nearest grid cell lying entirely downwind of the surface from which vorticity is being shed.

There is, of couse, a certain arbitrariness in this prescription. We trust that the vortex shedding process is self-equilibrating, such that shed vorticity erases singularities near edges and proceeds independently of fine details near the edges. Viscous flow analyses or comparison with experiments will be needed to validate that trust.

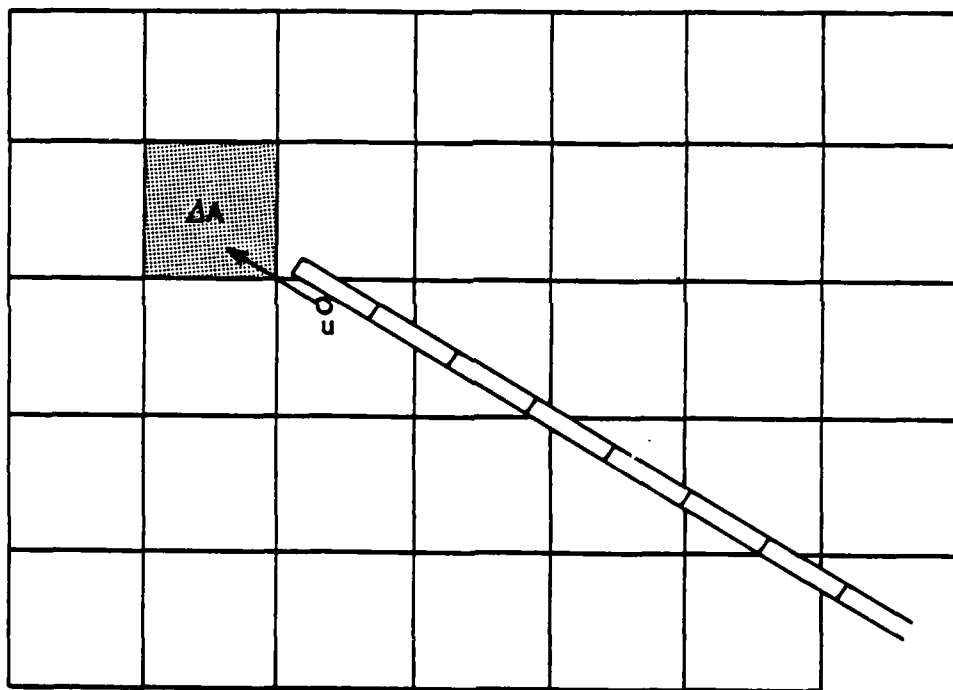


Figure 2.5. Means for deciding where free vorticity is placed in computational grid.

3. Numerical Methods for Two-dimensional, Unsteady, Separated Flow

a. Introduction

Methods for numerical modeling of lift-generated vortex flows can be roughly divided into those methods that employ discrete elements for free vorticity, as, for example, Geising (1968), and Hoeijmaker and Vaatstra (1983) and those that represent free vorticity as a continuous field, as, for example, Rizzi and Eriksson (1984). We have chosen to represent vorticity as a continuous field largely because we had much greater confidence in the stability, accuracy, and physical reasonableness of solutions produced by Euler solvers than in those produced by discrete element methods.

Given the choice of a continuous field representation for free vorticity, a complete predictive code for two-dimensional, unsteady, separated flow will have three ingredients:

1. A means for representing the effect of a solid obstacle on the flow velocity,
2. A means for shedding vorticity from the body into the free vorticity field, and
3. A means for advecting the free vorticity.

The third ingredient can be, and for our work is, a garden-variety Euler solver. The first and third ingredients may be combined in a code that employs body-fitted coordinates, but, as we shall see, it is possible to build a code that models arbitrary bodies without the complexities of body fitted coordinates. The third ingredient being the foundation upon which the whole is built, we proceed with a brief description of the Euler solver.

b. Advection of Free Vorticity

We have taken, as the starting point for our work, the Poseidon Hydro code, developed originally in 1976 for the simulation of two dimensional vortex flows in stratified fluid. The code has been extensively exercised, validated, and refined under a variety of programs for DARPA and for the U. S. Navy, but the only unclassified description of the code and its applications is given by St. Cyr (1980). The code has, over the years, acquired many special features directed toward the programs for which it was exercised. Our first step under the current program was to gather only the essential nucleus of this software into an entirely new code. We used an established test case (a vortex pair in unstratified, inviscid, incompressible fluid) to verify that the "new" code reproduced exactly the unstratified, inviscid dynamics of the Hydro code. This done, we had a code which had all the advantages of many years of testing behind it, but without the breadboard additions that old codes inevitably acquire.

The Hydro code, and its descendant, LIFTER, are formulated in terms of vorticity and streamfunction. This formulation has many nice features for two dimensional flow and is by far the most popular formulation for two-dimensional incompressible flow codes. A code formulated in terms of vorticity and streamfunction has just two essential ingredients: a scheme for transporting vorticity, and a scheme for computing the streamfunction given the vorticity.

The advective transport scheme is a derivative of the original SHASTA scheme of Boris and Book (1973). SHASTA is monotonic for time steps such that the local Courant number is always less than 0.5. That is, transport never produces new local extrema in transported field quantities. Monotonicity is, in fact, the key design requirement for a whole class of schemes which have come to be called flux-corrected transport schemes, of which SHASTA is an example. SHASTA is as close to

being second order accurate in space as it is possible to be without sacrificing monotonicity and exhibits exceptionally small residual numerical diffusion. Most schemes that are formally second order accurate and stable are substantially more diffusive than SHASTA. The algorithm that is implemented in LIFTER differs from the original SHASTA only in that a slightly more accurate flux correction term is employed in LIFTER. Time differencing is done using a second order Runge-Kutta (predictor-corrector) scheme.

The streamfunction is computed from vorticity by solving a Poisson equation:

$$\nabla^2 \psi = -\omega .$$

Two issues must be dealt with in solving this equation: representation of an infinite domain on a finite grid and an efficient way of solving the difference equations. If all of the vorticity is captured within the computational domain, an infinite domain may be represented by computing the value of the streamfunction on the boundary of the computational domain using a discrete form of the Biot-Savart integral for the streamfunction, and then solving the Poisson equation subject to the computed Dirichlet boundary condition. This reasonable strategy was employed in the Hydro Code as described by St. Cyr (1980). We have subsequently adopted the approach of solving the Poisson Problem on a very large grid using fast Fourier transforms. Despite the fact that the computational domain must be substantially enlarged for this latter strategy, it is significantly faster than the original . The speed advantage arises because the operations count for the Biot-Savart integral is $O(N^3)$ while the operations count for the Fast Fourier Transform is $O(N \ln N)$. Furthermore, the Block Cyclic Reduction algorithm formerly used, while having an operations count that is $O(N \ln N)$, involves tridiagonal sweeps that do not vectorize on the CRAY.

c. Representation of Wing Sections by Bound Vorticity

The velocity field computed by the free vorticity code is different from the actual velocity field around a solid body by a flow which is everywhere irrotational except within the solid body. For our purposes, the solid body will always be a one-dimensional curve within the computational domain. In order to compute the actual velocity field, we must obtain a flow that is irrotational everywhere but along the curve and that cancels along the curve the normal velocity due to free vorticity.

There are a variety of techniques available to compute the required velocity field, but by far the most attractive are the so-called panel methods. These methods compute the required velocity field as if it resulted from a distribution of flow field singularities distributed along the body. The great power of these methods derives from the fact that the body is represented by polygonal elements, permitting the representation of nearly arbitrary geometries.

Of the many possible choices for the flow field singularities, by far the most natural for the problem at hand is a sheet of vorticity. Vortex sheet panel codes, as in Raj and Gray (1978), are a standard technique for the aerodynamics of thin airfoils.

Figure 3-1 illustrates most of the essential features of the panel code that has been embedded into lifer. The wing is represented as series of N panels of arbitrary length and orientation, each panel being a sheet of vorticity of constant, unknown strength. Panel α induces a normal velocity at a chosen control point on panel β ; the value of this velocity for unit vorticity per unit length on panel α is the influence coefficient $C_{\alpha\beta}$. The sum of all of the induced velocities at panel β must exactly cancel the normal velocity at panel β due to the free vorticity. We thus have N equations for the N unknown panel vortex strengths.

The matrix of influence coefficients computed by the preceding prescription will be numerically ill-conditioned, as a consequence of being nearly singular. This near singularity is a consequence of the exact singularity of the continuum integral equation being approximated. The singularity of the integral equation is reflection of the well-known fact that the flow around an airfoil can have an arbitrary net circulation. This indeterminacy is resolved in conventional aerodynamics by insisting that a stagnation point coincide with the sharp trailing edge of an airfoil. This requirement is commonly known as the Kutta condition.

If the flow around the airfoil is permitted to separate, the arguments that lead to the Kutta condition fall apart. From the absolutely fundamental Kelvin circulation theorem, we know that the total circulation of the flow must be preserved. If we start with an airfoil at rest, then the indeterminacy is resolved by insisting the total circulation of the flow be zero. This condition, which we have chosen to call the Kelvin condition, is used to replace one of the rows in the matrix of influence coefficients.

All that has been said so far is reasonable and even obvious, but some details have been glossed over. For example, the most obvious choice of control points, the center of each panel, produces an oscillating distribution of bound vorticity on a flat plate in a uniform free stream. Moving the control point to the quarter chord of each panel results in a vorticity distribution that more nearly approximates the known solution to the continuum equations. This naturally begs the question as to why the quarter chord and not the three quarter chord? Or, to put it another way, what is the difference between the quarter chord and the three quarter chord for a flat plate at 90 degrees angle of attack? Similarly, which of the equations is to be replaced by the Kelvin condition?

We have alleviated the arbitrariness of the choice, at least to some extent, by solving for the bound vorticity with one arbitrary choice of control points and for its mirror image, and then averaging the results. The Kelvin condition in each case replaces a control point equation at one end of the panel. While the choices are still arbitrary, the procedure at least preserves any symmetries the problem may have had before discretization.

A further detail we must deal with is that once we have the singularity distribution, we must compute the velocity field due to the singularity distribution at every point in the computational grid. Calculating this velocity field from a Biot-Savart integral is impractical, not only because of the operation count, but also because an impracticably large number of influence coefficients would have to be stored. The most economical way to generate a velocity field from the bound vorticity is to assign the bound vorticity to grid points and solve a Poisson equation as for the streamfunction due to free vorticity. This seemingly crude procedure seems to yield remarkably good results as will be evident from the streamfunction plots in Chapter 4.

d. Conversion of Bound Vorticity into Free Vorticity

In Chapter Two, we discussed at length the physics of our model for vorticity shedding. Here it remains only to report on the details of the method by which this shedding model is implemented. The mean velocity at the wingtip is computed by interpolating the velocity field on the grid, and subtracting the velocity of the wingtip, if the wingtip is not stationary in the grid. The vorticity on the end panel is presumed not to contribute to the mean velocity at the wingtip. The mean tangent velocity is computed by dotting the mean velocity with an outward facing unit tangent vector. The tangent velocity on one side of the wing is taken to be the mean tangent velocity plus $\gamma/2$ and the tangent velocity on the other side of the wing is taken to be the mean tangent

velocity minus $\gamma/2$, where γ is the bound vorticity at the wingtip. Given the velocity on either side of the wing, it is a straightforward matter to compute the rate of shedding from the formulas in figure 2.4.

Once the rate of shedding has been computed, the vorticity is added to the free vorticity in the grid. In order to ensure that the newly freed vorticity is not trapped at the wingtip, the vorticity is added to a control volume that does not contain the wingtip.

This description makes clear a possible weak point in the model. The rate of vorticity shedding is proportional to the value of the vorticity on the last panel. For an impulsively started flat plate, the vorticity at the end of the plate is infinite, and yet the rate of vorticity shedding computed by our model is dependent upon the artificially finite value computed as a result of the discretization process. The only reason to believe that such an arbitrary procedure could yield correct results is that the process is self-correcting. That is, one effect of shedding vorticity is to relieve the singularity at the wingtip. If too small an amount of vorticity is shed, the rate of shedding at the next time step will be larger. If too large an amount of vorticity, is shed, the rate of shedding will be smaller. This kind of feedback mechanism suggests the existence of stability criteria relating the grid cell, wing panel, and time step size. We have not yet tested the possible dependence of gross predictions, such as aerodynamic coefficients, on the wing panelization.

4. Computational Results for Two-dimensional, Unsteady, Separated Flow

a. Impulsively Started Flat Plate at 90 degrees Angle of Attack

The first problem for which we exercised LIFTER was a flat plate at 90 degrees angle of attack. The chosen grid was 40 by 40 cells, and the flat plate was represented by 22 panels of equal length.

Figure 4.1 presents the normal force coefficient history as predicted by LIFTER compared with the measured average value (Hoerner, 1975, p. 21-1) and with the prediction of the Helmholtz model (op. cit.). There are no time dependent measurements of the force history on a flat plate that are known to us. Beyond a large starting transient in the normal force, there is no evidence of oscillatory behavior in the force coefficient that would be indicative of the formation of a vortex street. In fact, for the time simulated, the force coefficient decreases monotonically with time, as would be indicative of the formation of a stable recirculation cell.

Figure 4.2 presents a series of comparisons of computed streamlines with aluminum particle streakline photographs and Taneda and Honji 1971. We can expect the comparison between instantaneous streamlines and streaklines to be reasonable if the exposure time of the photograph is short compared to a characteristic time for the unsteadiness of the flow. Taneda and Honji do not state the exposure time for their photographs, although we may presumably infer that it is less than the spacing of their photographs in time, typically 0.5 B/U. The blockage factor, that is the width of the plate over that width of the test channel, was less than 10%.

The qualitative behavior of the computed streamlines compares well with the streakline photographs over the entire series of comparisons,

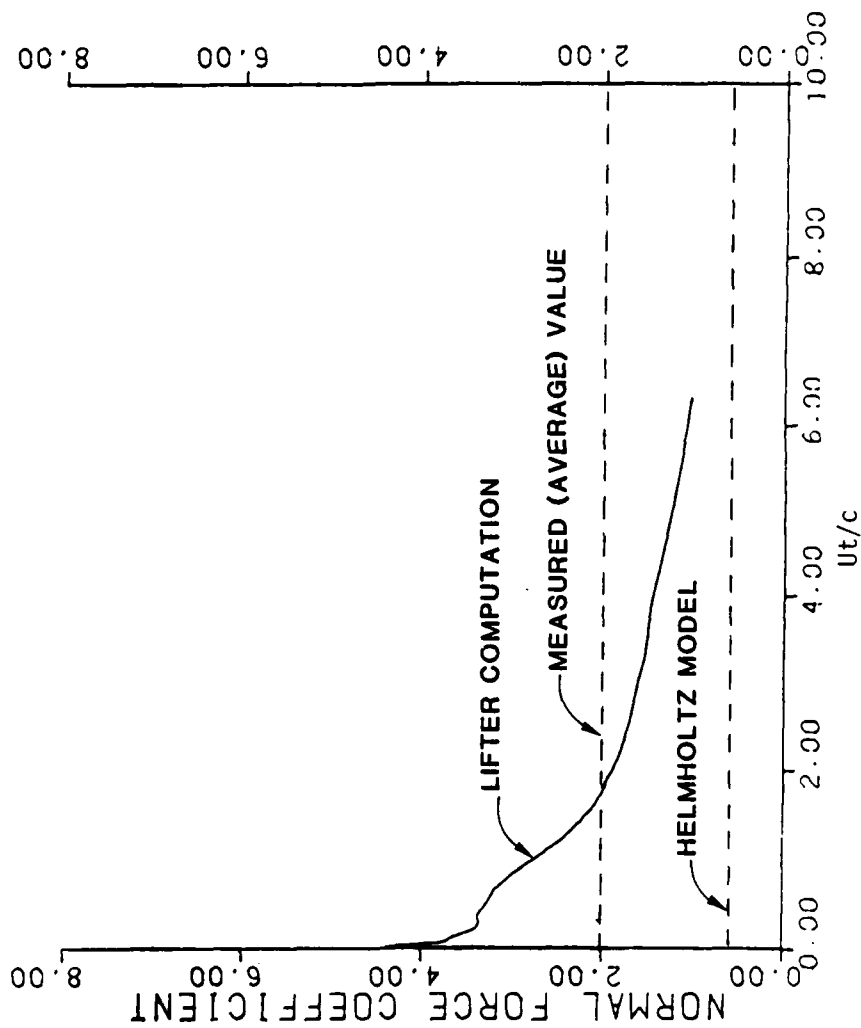
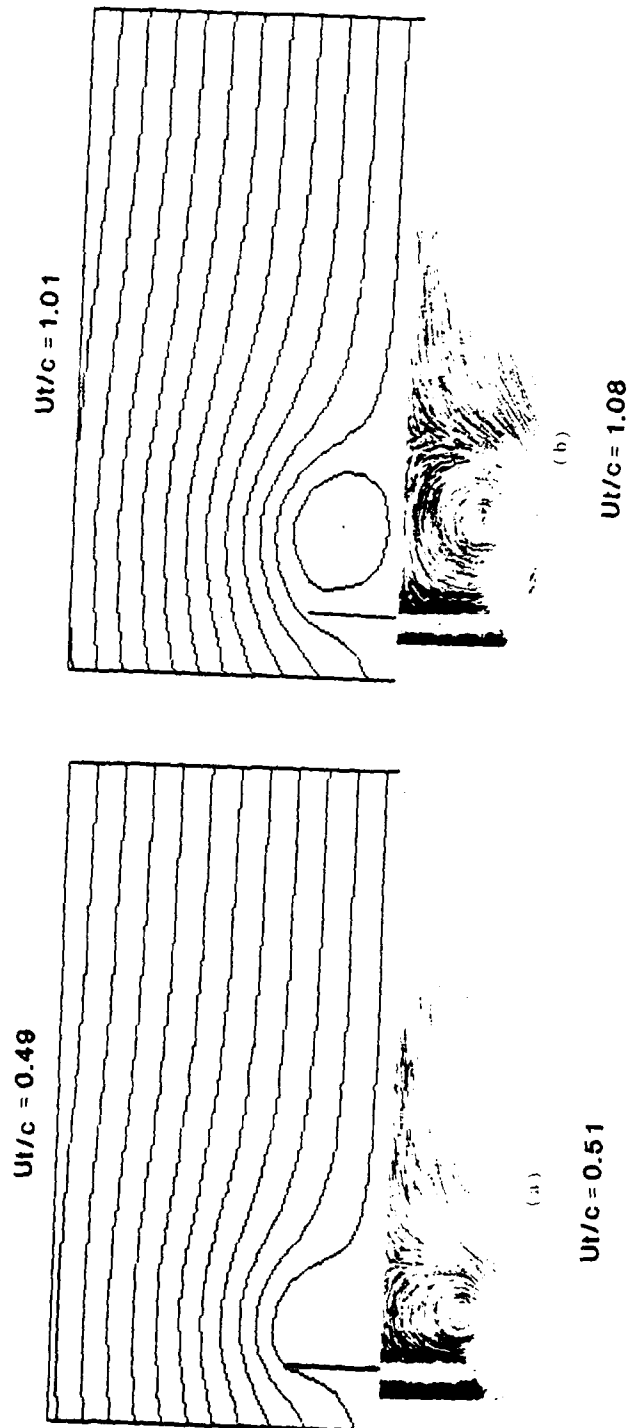


Figure 4.1. Computed normal force coefficient for a flat plate at 90° angle of attack.

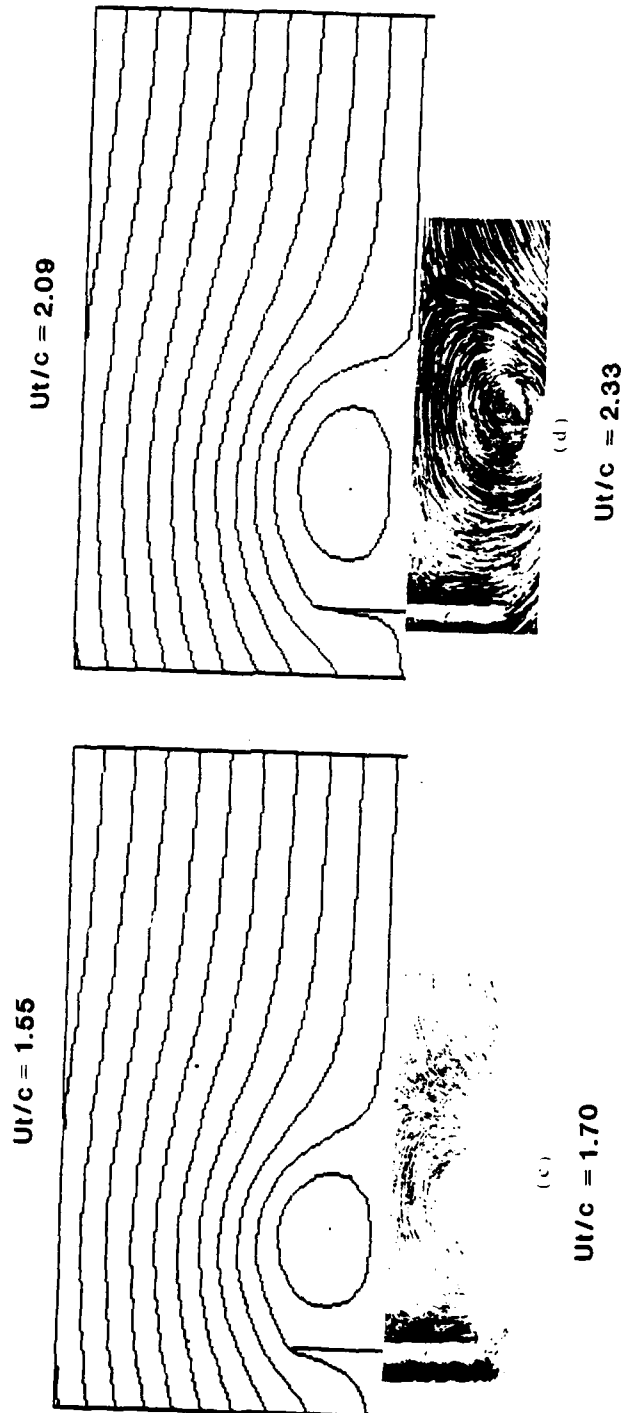
LIFTER



Taneda and Honji (1971)

Figure 4.2 a, b. Impulsively started flat plate at 90° angle of attack. Comparison of computed streamlines with streakline photographs.

LIFTER

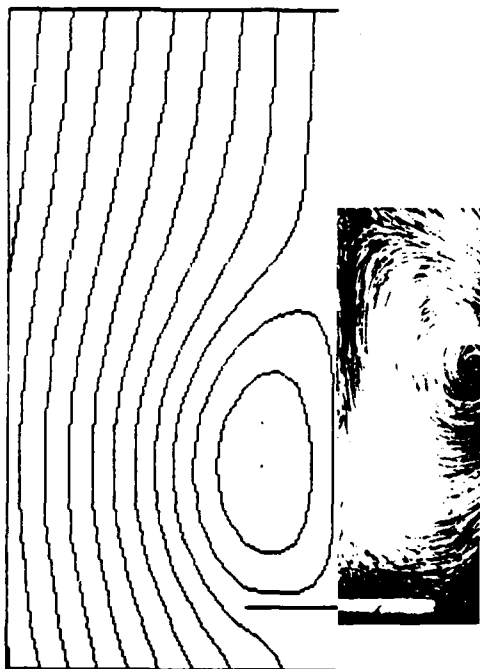


Taneda and Honji (1971)

Figure 4.2 c, d. Impulsively started flat plate at 90° angle of attack. Comparison of computed streamlines with streakline photographs.

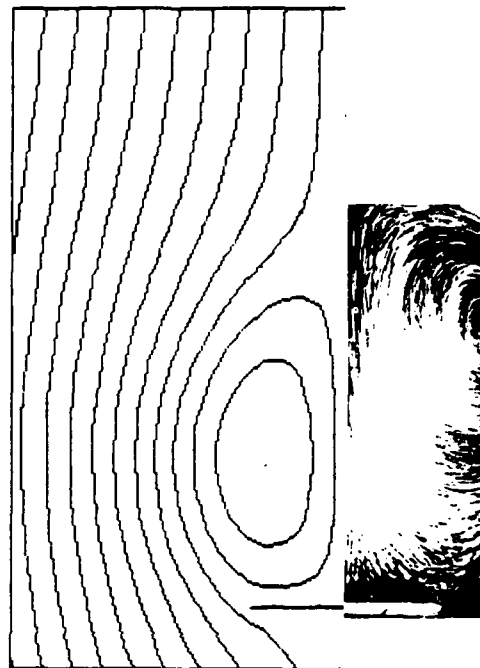
LIFTER

$U/c = 3.20$



$U/c = 3.07$

$U/c = 3.74$



$U/c = 3.77$

Taneda and Honji (1971)

Figure 4.2 e, f. Impulsively started flat plate at 90° angle of attack. Comparison of computed streamlines with streakline photographs.

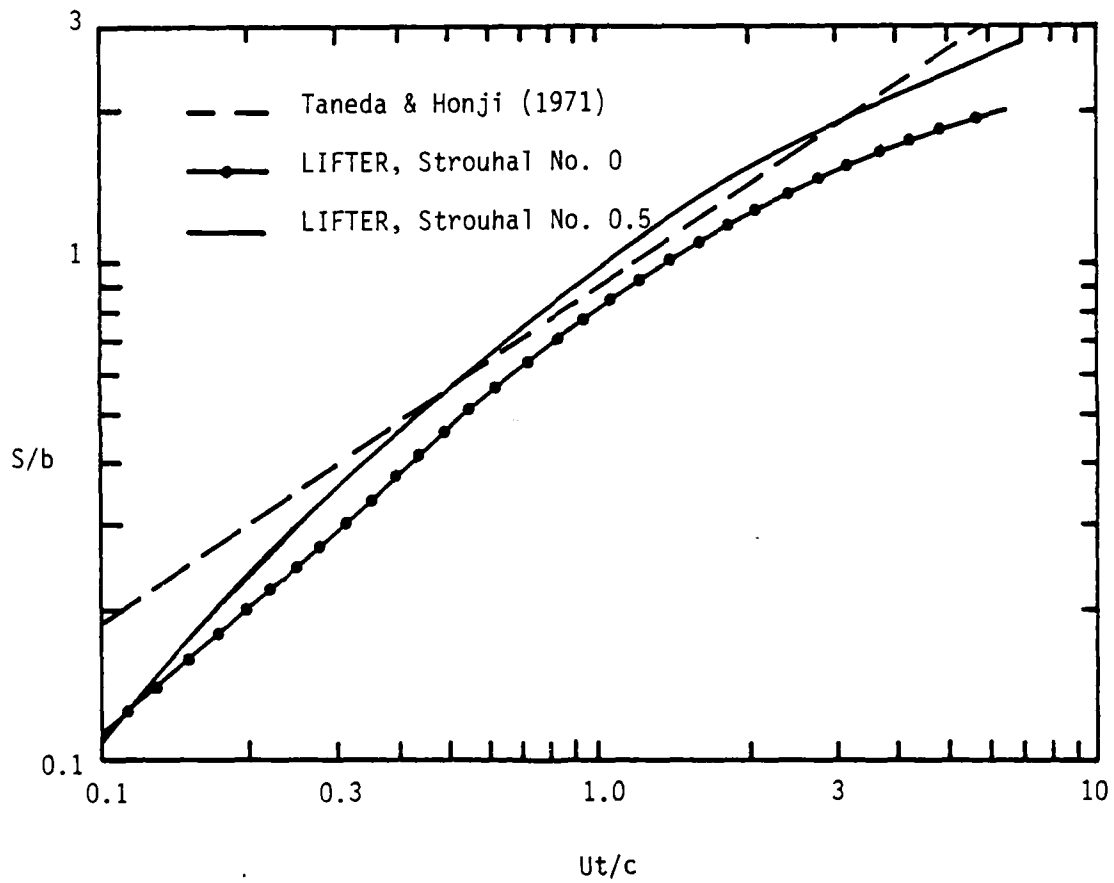


Figure 4.3. Length of recirculation cell from measurement and from computation.

but the recirculation cell from the LIFTER simulation grows significantly more slowly than the recirculation cell in the streakline photographs. Figure 4.3 makes a more quantitative comparison. Taneda and Honji have inferred the relation

$$s/c = 0.89(Ut/c)^{2/3}$$

where s is the length of the recirculation cell and c is the chord of the plate. Figure 4.3 compares this relation with the length of the recirculation cell from LIFTER as inferred by taking twice the distance from the plate of the centroid of the vorticity in half the recirculation cell. The prediction from LIFTER does not follow the simple power law relationship inferred by Taneda and Honji, but rather grows at first more quickly and then more slowly than the inferred experimental relationship. Figure 4.3 also contains results for an oscillating chord, to be discussed in section C.

Both the photographs and the computed streamlines confirm the existence of a stable recirculation cell over the entire length of the LIFTER simulation. For large Reynolds numbers, we infer from figure 10 of Taneda and Honji an inviscid scaling for the critical time:

$$t_{cr} = 5.3(c/U) .$$

While the determination of this time from streakline photographs obviously involves some subjective judgment, we may expect that the LIFTER computation was simply too short to exhibit breakdown of the recirculation cell and consequent rebounding of the force coefficient from its monotonic decline. It also is not clear, from the paper of Taneda and Honji, whether the initial breakup of the recirculation cell is a two or three dimensional phenomenon.

It would have, of course, been desirable to have a longer simulation, but, because of the Kelvin condition and because of the moment calculation, both of which involve integration over the entire field of vorticity, we are currently forced to stop our simulations when significant vorticity leaks from the edge of the computational domain. We will discuss the economics of these computations further in Chapter Five.

Figure 4.4 presents plots of the bound vorticity as computed by LIFTER at various times. Of these, the only one that is readily interpretable is at $t = 0$, where the exact solution is known for the bound vorticity on a flat plate in uniform flow. This result is derived in Appendix B. The distribution of bound vorticity computed by LIFTER agrees well with the theoretical prediction for all but the last two panels, where the assumed constant distribution of vorticity is a poor approximation to the square root singularity. It can also be seen from figure 4.4 that the separated vortex flow almost immediately reduces the bound vorticity to a small fraction of its initial value. The residual concentration of bound vorticity at the end of the wing is of some interest. We will speculate as to the meaning of this phenomenon in the last section of this chapter.

The conclusions we may draw from this first comparison of the predictions of LIFTER with experimental data are not as strong as we would like. The qualitative behavior of the code predictions is certainly reasonable. The quantitative behavior of the recirculation cell is at least not grossly inconsistent with the results of measurements. We would most like to make a comparison between the measured and predicted average normal force coefficients, but this comparison will require a much longer computation than the one presented here.

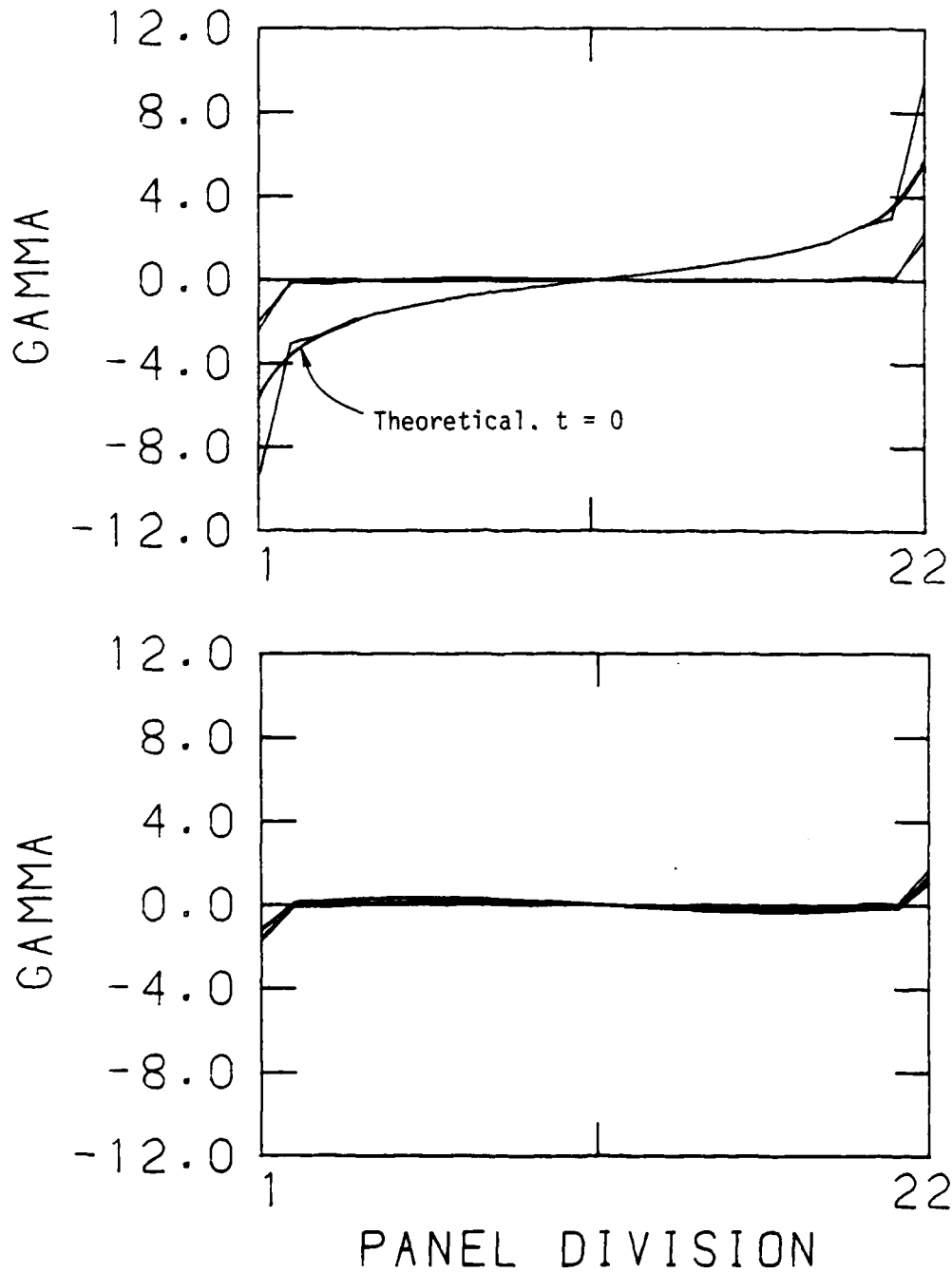


Figure 4.4. Impulsively started flat plate at 90° angle of attack.
Chordwise distribution of bound vorticity, at various times.

b. Impulsively Started Flat Plate at 45 Degrees Angle of Attack

Despite the fundamental importance of the flat plate at 90 degrees angle of attack to an understanding of post-stall aerodynamics, the problem is peculiar because of its symmetry. In order for a vortex street to appear, it is necessary for some symmetry-breaking instability to develop. For a flat plate at any other angle of attack, asymmetric shedding will begin immediately, so that the formation of a long-lived recirculation cell is unlikely.

Figure 4.5 presents a sequence of vorticity maps from our next exercise for LIFTER, a flat plate at 45 degrees angle of attack. It seems a shame to belabor the elegance of the simple physics in this figure with technical comment. It must be noted that the aspect ratio of the plots is not quite right; the dots along the border of the plots should be equally spaced, but they are not.

Figure 4.6 presents another striking plot from the same simulation, this time of the absolute value of vorticity, and this time with the aspect ratio correctly represented. Next to it is an aluminum flake flow visualization of the same problem, reproduced from Cantwell (1981). Although the photograph is obviously in a much later state of development, the similarity of flow patterns is gratifying. The shedding frequency in the numerical simulation is obviously very close to the shedding frequency of the real flow.

Figure 4.7 presents the force coefficient history from this simulation, and here we begin to see the kind of effects we expect from the formation of a vortex street. Comparison of the force coefficient history with the flow maps shows that the shedding process has completed just slightly more than one complete cycle at the end of the simulation where the normal force coefficient is rising.

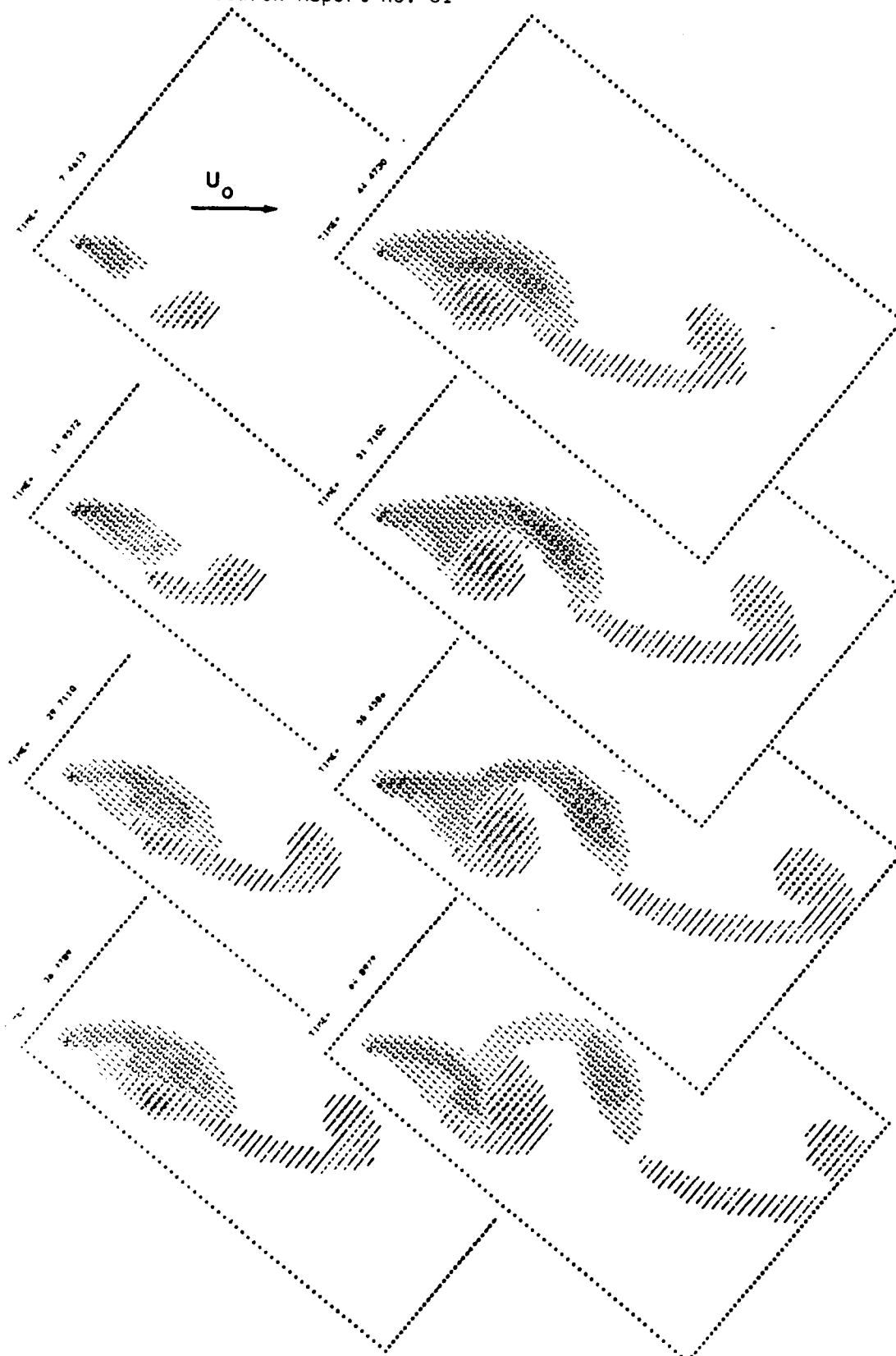
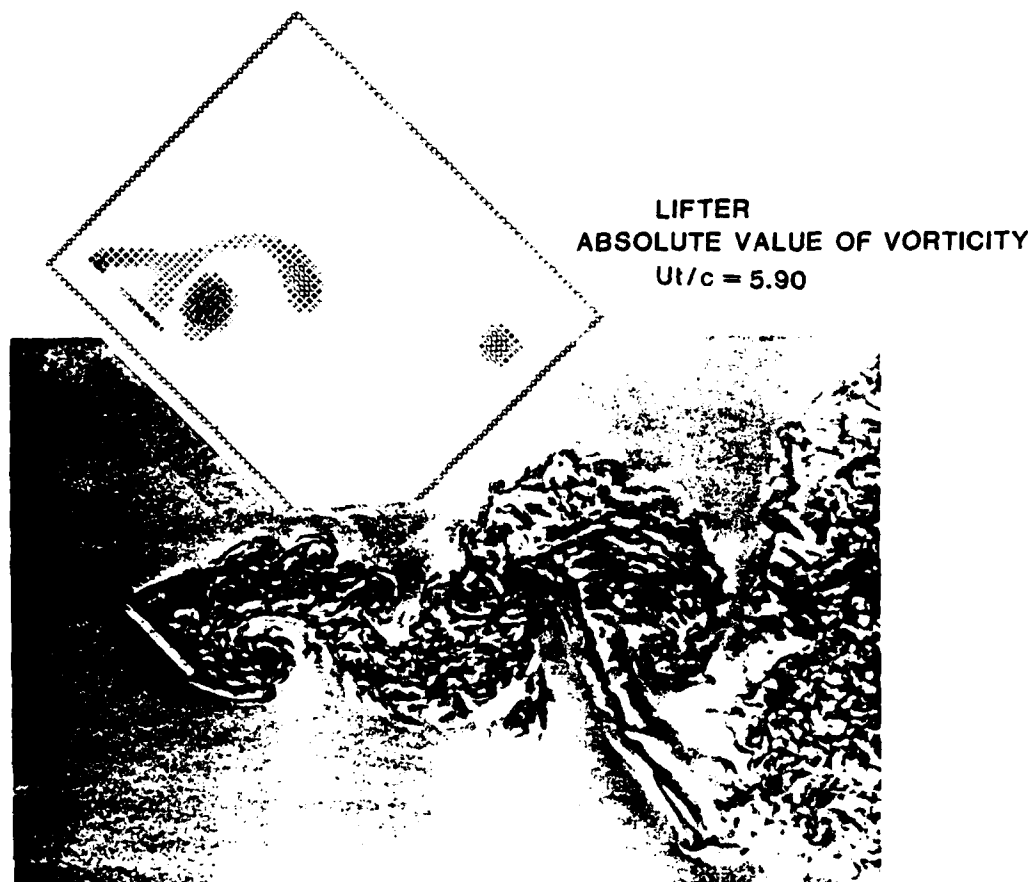


Figure 4.5. Distribution of vorticity for an impulsively started flat plate at 45° angle of attack.



ALUMINUM FLAKE FLOW VISUALIZATION
(Cantwell, 1981)

Figure 4.6. Flat plate at 45° angle of attack. Comparison of computed distribution of absolute value of vorticity with aluminum flake flow visualization.

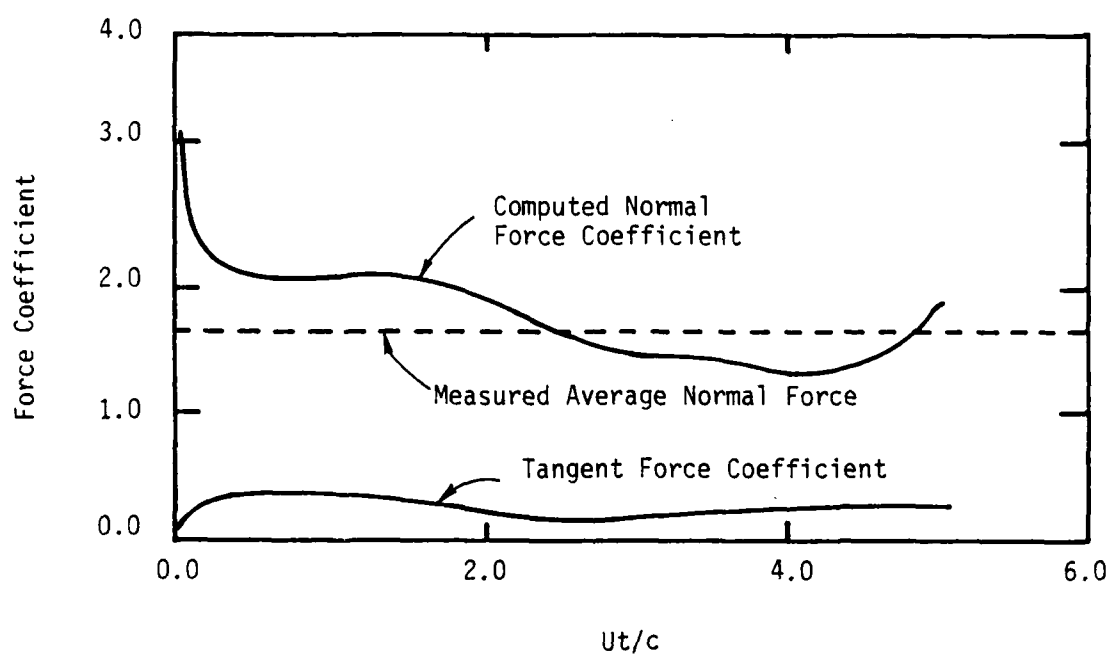


Figure 4.7. Impulsively started flat plate at 45° angle of attack: force coefficient histories.

Figure 4.7 also shows some unexpected, and -- perhaps -- disquieting physics in the form of a significant tangent force! The calculation having been done with an ostensibly inviscid code, the circumspect numerical modeler would perhaps have done better to have left this curve off the plot, but there it is, and it deserves some explanation. First, of course, is the possibility that this prediction is simply the result of some modeling inaccuracy. After all, despite the intuitively obvious fact that the tangent force on a flat plate in inviscid flow should be zero, that this should be so in the numerical simulation requires the vanishing of a time derivative of a particular moment of vorticity, with no obvious symmetry in the problem to enforce this condition.

It is a prediction of ideal fluid mechanics that there is no net force whatever on a closed body in a uniform freestream. In order to explain lift and drag and in order to predict them with LIFTER, we must introduce viscous mechanisms, by whatever circuitous route. In classical aerodynamics, the magical device is the Kutta condition, in LIFTER, it is the shedding mechanism. The theorems used to compute forces in LIFTER remain valid if viscosity is included, and LIFTER contains mechanisms that are manifestly viscous. There is, then, no good reason to dismiss the predicted tangent force as either physically or mathematically incorrect.

The distribution of bound vorticity, presented in figure 4.8, shows no new surprises. The vorticity at the trailing edge bounces up and down with the cyclic shedding process. As in the plate at 90 degrees angle of attack, there remains a large concentration of bound vorticity at the leading edge throughout the simulation.

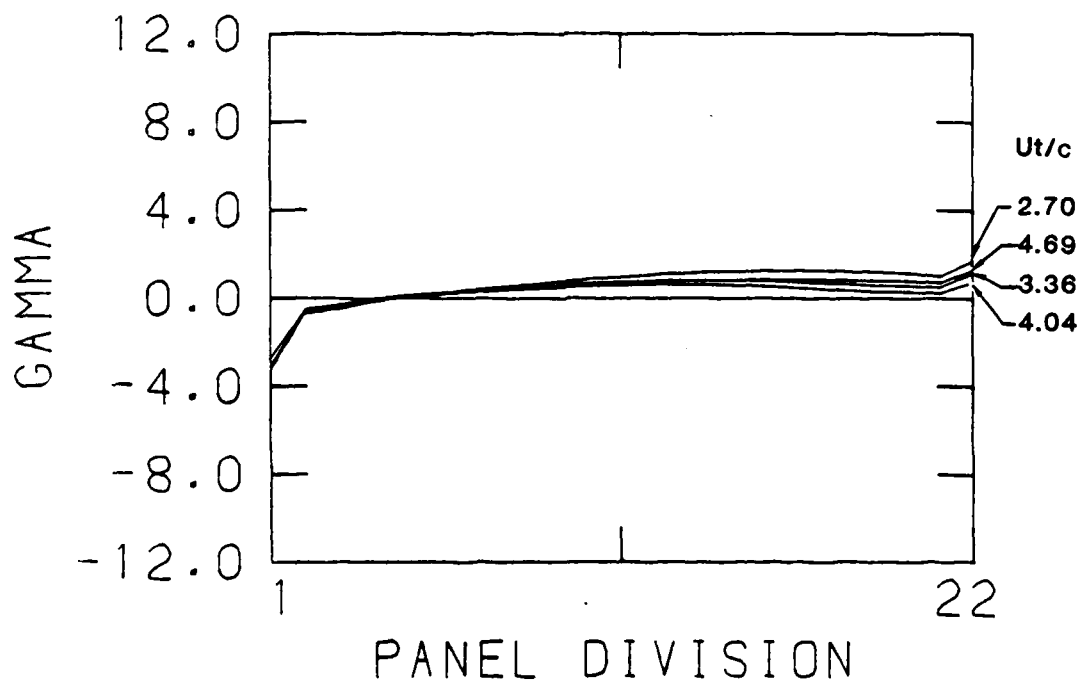
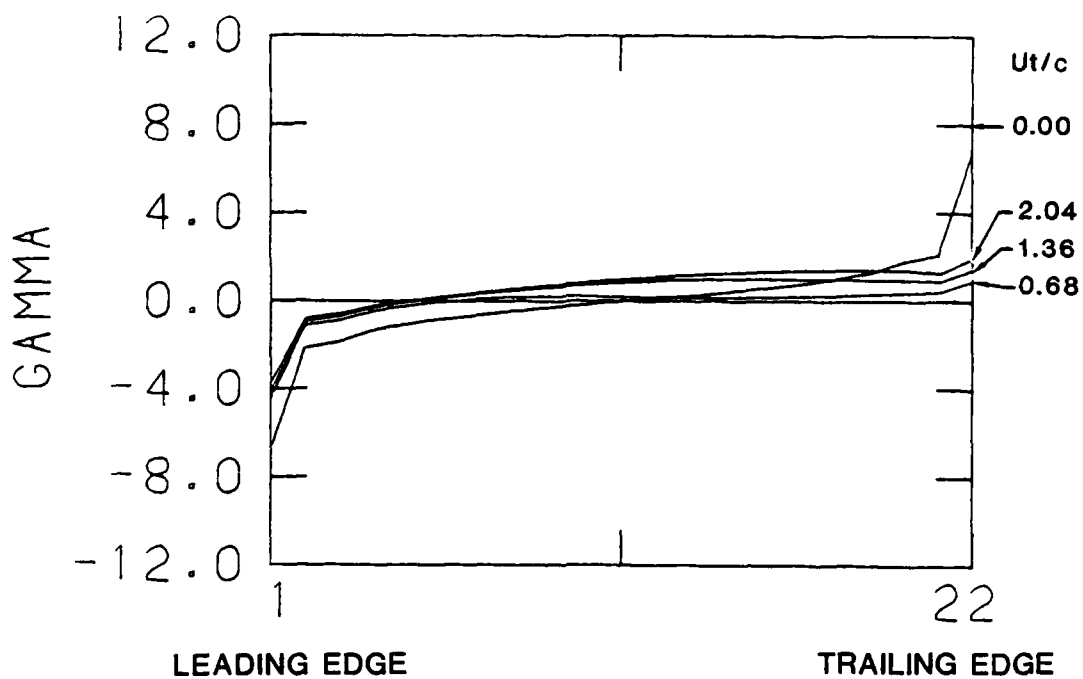


Figure 4.8. Chordwise distribution of bound vorticity for an impulsively started plate at 45° angle of attack.

c. Impulsively Started Flat Plate with Oscillating Cross Section
at 90 Degrees Angle of Attack

The first two problems in this section are important from the point of view of understanding and validating the basic model. The underlying motivation for the current program is the desire to achieve sufficient active control of the shedding process as to have significant control over the net forces on a stalled aerodynamic shape. We felt that it was desirable to get results as early as possible that would indicate the feasibility of controlling the aerodynamics through manipulation of the salient edges, whether through oscillating jet flaps or oscillating mechanical flaps.

With this end in mind, we have performed two simulations of flat panels with oscillating chord at ninety degrees angle of attack. The Strouhal number (the ratio of the oscillation frequency to the convective time scale based on chord) was chosen to be two for one of the runs and 0.5 for the other. The amplitude of oscillation in both cases was 10% of the chord (that is, the maximum total chord is 1.1 times the minimum total chord).

The results of these simulations are presented in figures 4.9-4.10. The normal force coefficient history for the Strouhal number 2 case, presented in figure 4.10 is in striking contrast to the Strouhal number 0 case previously presented in figure 4.1. Not only the peak normal force coefficient, but also the mean normal force coefficient is significantly enhanced by the oscillating chord. The normal force coefficient history for the Strouhal number one half case also shows augmented mean lift, but the augmentation is considerably less striking than for the Strouhal number 2 case.

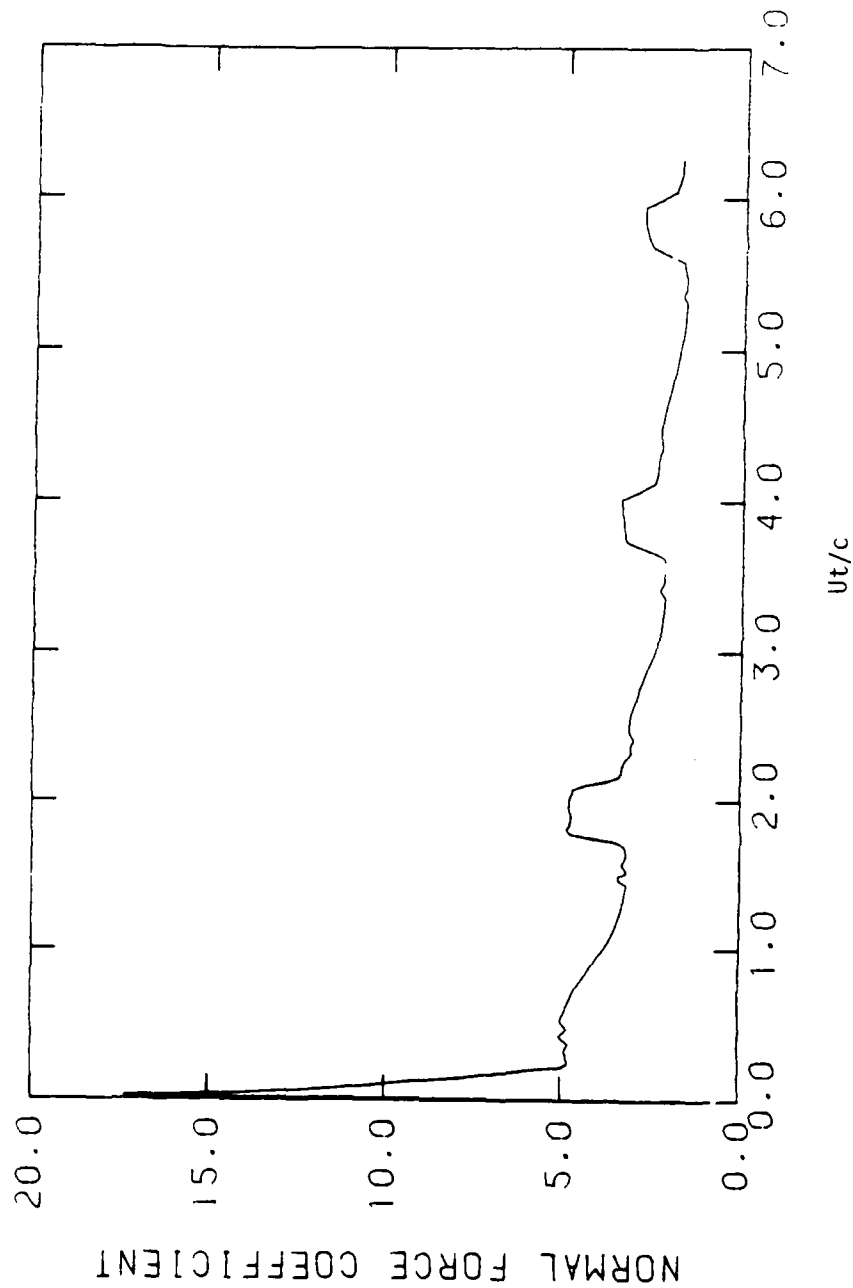


Figure 4.9. Normal force coefficient history for an impulsively started flat plate with oscillating chord. Strouhal number = 0.5.

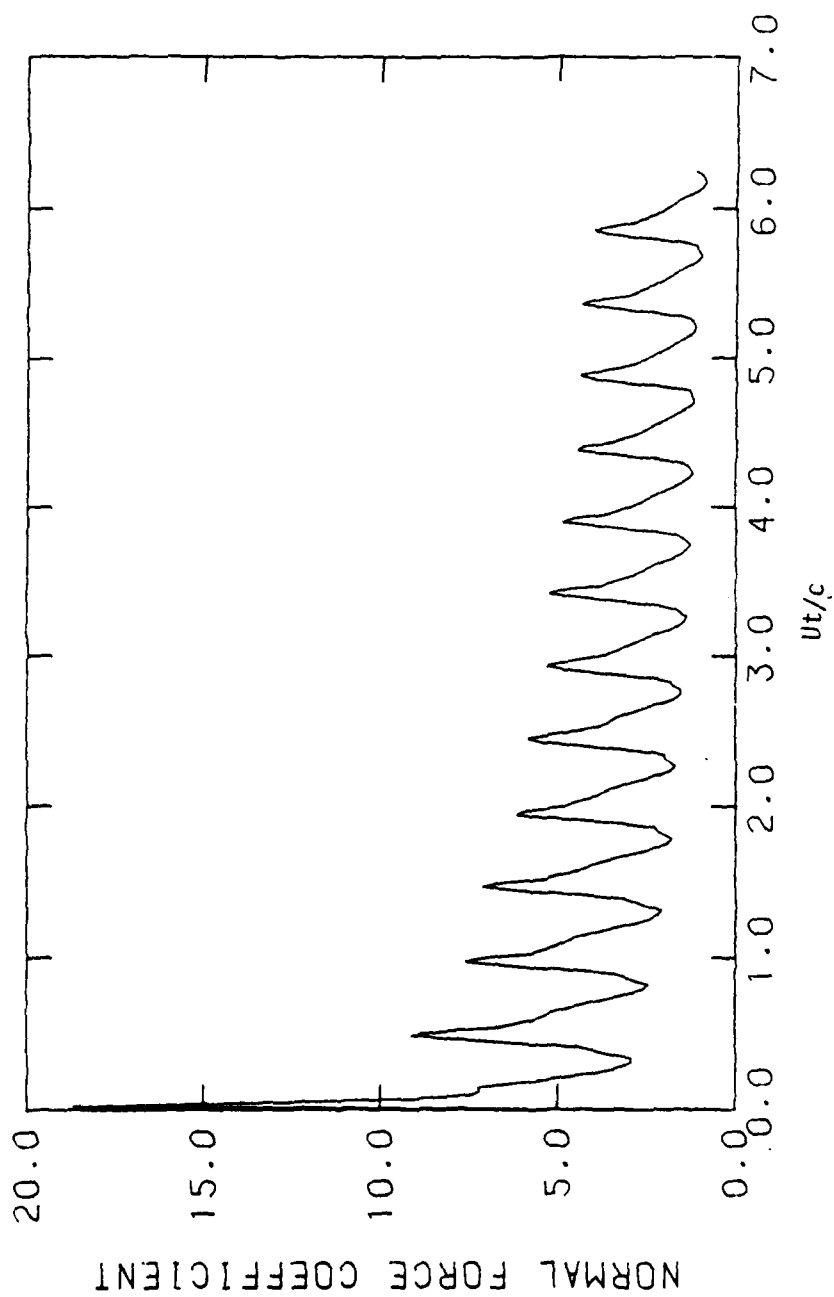


Figure 4.10. Normal force coefficient history for an impulsively started flat plate with oscillating chord. Strouhal number = 2.

Referring back to figure 4.3, we also see that the recirculation cell for the plate with oscillating chord grows faster than for the plate with fixed chord.

We would expect, even for an unseparated flow, a significant effect from oscillating the chord, if only from acceleration and deceleration of the changing virtual mass associated with the changing chord. The virtual mass associated with a flat plate may be readily inferred from Batchelor (1967) p. 431, equation (6.6.19) to be $\pi \rho c^2/4$. The force associated with the oscillation of the virtual mass is given by

$$\begin{aligned} \frac{\partial}{\partial t} (\pi \rho c^2 U/4) &= \frac{1}{2} \rho U \pi^2 f c^2 (2A \sin(2\pi f t) \\ &\quad + 2A^2 \cos(2\pi f t) \sin(2\pi f t)) \end{aligned}$$

The normal force coefficient associated with the virtual mass is then given, for small amplitude oscillations, by

$$2\pi^2 (f c/U) A \sin(2\pi f t) = 2\pi^2 St A \sin(2\pi f t)$$

which, for a Strouhal number of two yields an envelope amplitude of roughly 4 with an amplitude of 0.1, and an envelope amplitude of roughly 2 for the same amplitude and a Strouhal number of 0.5. These numbers are not necessarily valid when the flow is separated, as in our calculations, but they agree reasonably well with the envelope of the oscillating component of the computed normal force coefficient.

There appears to be significant (greater than fifty percent) augmentation of the mean normal force coefficients for the cases with the oscillating chord as compared to the plate with fixed chord. The mean for all three cases has dropped at a non-dimensional time of 6 below the measured average normal force coefficient for a flat plate at 90 degrees angle of attack.

d. Conclusions from Two-Dimensional Simulations

Having presented our results, let us now recapitulate and examine the evidence. Two questions should be answered:

1. Is the model reasonable in the sense that it adequately predicts reality?
2. What have we learned about separated flow?

In answering the first question, we must admit that the evidence at our disposal is not entirely satisfactory in that the runs are shorter than those we would like to be able to examine. Only in one case, the flat plate at 45 degrees angle of attack, do we see the kind of periodic shedding that we expect is responsible for the failure of potential flow and Helmholtz models to predict the measured drag coefficient of a flat plate. Even in that case, we have barely one full cycle of the periodic process to examine, a situation that makes it difficult to draw conclusions about the mean behavior of the system. Nevertheless, it is easy to believe that the normal force coefficient in figure 4.7 is oscillating about the correct mean value.

The qualitative agreement of the computed wake of the flat plate at forty five degrees angle of attack is certainly evidence that the model not only predicts the periodic shedding process, but does so correctly.

The only time dependent data available to us are the flow visualization experiments of Tonedá and Honji. For the flat plate at normal incidence, the persistence of a stable recirculation cell is evident in the flow visualizations of Tonedá and Honji, but, based on inviscid scaling, the computed recirculation cell grows more slowly longer than in the experiments.

Some features of the predictions are not necessarily contradicted by observation, but certainly run contrary to expectations. The prediction of significant tangent force coefficient for the flat plate at forty five degrees angle of attack must be included in this category, as must be the not unrelated phenomenon of a persistent leading edge singularity for this calculation.

We have learned from this series of simulations that a model of vortex shedding that ignores the details of the boundary layer is capable of making reasonable predictions of the shedding process. Unlike some other models, our model does not predict instantaneous relief of edge singularities, but rather that reversed flow persists for some time.

We have also learned that periodic forcing, such as might be induced by jet flaps, enhances both the rate of shedding and the mean lift coefficient.

5. Directions for Further Work in Two Dimensions

a. Code Modifications Aimed at Economics

We have been limited, in our first series of simulations, by the need to capture the entire field of shed vorticity. This need has arisen both because of the Kelvin condition, and because of our use of the vorticity theorems of Chapter 1 for the computation of aerodynamic forces. We can easily keep track of vorticity leaving the computational domain for purposes of enforcing the Kelvin condition. We cannot keep track of the x and y moments of vorticity leaving the computational domain without further assumptions, such as assuming that the vorticity simply convects with the free stream velocity. Such modifications will be worthwhile only if we wish to make very long simulations.

The cost of running the LIFTER is currently dominated by the cost of solving the linear system of equations for bound vorticity. The solver currently in use for this purpose uses Gauss elimination with pivoting. Simply switching to a more highly optimized solver will be the most cost effective step we can make in obtaining longer runs at an acceptable cost.

b. Calculations Aimed at Further Understanding of the Computational Model

We have so far been unable, because of costs, to check the dependency of results on wing panelization. We shall surely wish to perform such an experiment when more efficient software for computing bound vorticity is in place.

We may also wish to check the dependency of results on the details of the vortex shedding model by ignoring vorticity swept off the lee

side when the flow at the edge is outward on both the windward and leeward side of the wing.

c. Calculations Aimed at Further Understanding of the Physics
and of the Model

We would of course, like to see the model duplicate average drag coefficients for flat plates, and to do this, we expect to need much longer runs than those presented in Chapter 4. Toned and Honji mention that the breakdown of the recirculation cell is an unsymmetrical process. Such an asymmetry must correspond to an instability of some kind. Whether, when, and how such an instability might arise in a two-dimensional numerical experiment present interesting question. The free vortex sheet may also exhibit a symmetrical instability.

We shall, of course, want to simulate a slender delta wing at angle of attack. These simulations will provide us with a further opportunity to compare the model with measurements.

The ultimate goal, of course, is to obtain predictions that are relevant to active vortex control. We have made tentative steps in this direction with the runs reported in Chapter 4, but we shall surely want more extensive results in this area.

6. Numerical Methods for Three Dimensional Unsteady Flow

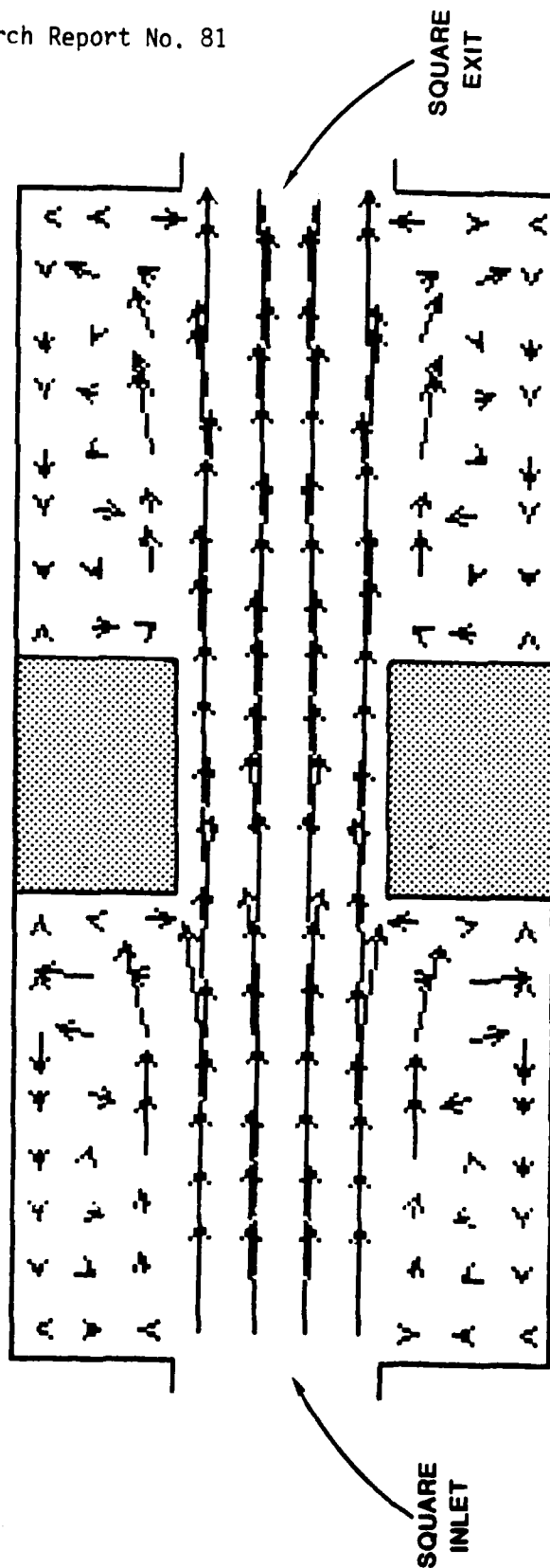
The two dimensional work presented so far is, more than anything else, preliminary work aimed at implementing a three dimensional model. The understanding we have achieved as a result of the two dimensional work reported here has carried us a considerable distance in that direction.

The ingredients for a three dimensional model are much the same as the ingredients for a two dimensional model: an Euler solver, a means for enforcing zero normal velocity on embedded surfaces, and a means for shedding vorticity.

Euler solvers for incompressible, three-dimensional flow are considerably less common than for incompressible, two-dimensional flow. Poseidon Research has recently developed one such code, and this code appears to be well suited as a starting point for a three-dimensional version of LIFTER.

Like LIFTER, Burner uses flux-corrected transport for the advection step. Unlike LIFTER, Burner is formulated with three components of velocity as the fundamental field quantities. The fact that Burner does not explicitly conserve vorticity works to our advantage. In particular, flows simulated by Burner will separate without the inclusion of an explicit shedding mechanism. Figure 6.1 presents a field of flow vectors obtained by simulating a square jet in a square channel with a square obstruction midway down the channel. The square obstruction is simulated by adding impulsive forces to the model system. The flow separates both at the inlet and at the square obstruction.

We would simulate the presence of embedded surfaces for aerodynamic calculations in much the same way. We would calculate impulsive forces that cancel the normal velocity at the embedded surface. Just as for



HORIZONTAL VELOCITIES IN HORIZONTAL MIDPLANE

Figure 6.1. Euler code simulation of a separated three-dimensional flow square jet in square channel with obstruction.

bound vorticity, the effect of the impulsive forces is non-local, and calculation of these forces requires the solution of a set of linear equations. Application of the local effect of the impulses will produce a velocity field that is neither incompressible nor zero at the embedded surface. The solution is completed by solving a Poisson equation for a velocity potential whose gradient, when added to the velocity field, will result in a velocity field with all of the desired characteristics.

It is a pleasant circumstance that most of this technology is already in place, and that the only new software required will be software to solve for the panel impulses.

Although we are confident that embedded surfaces will shed vorticity, it is by no means clear that they will do so correctly. Exploring the actual mechanism by which the code produces shed vorticity, and its correctness, will constitute a significant part of the development effort.

References

Batchelor, C. K. 1967 An introduction to fluid dynamics. Cambridge: The University Press.

Geising, Joseph P. 1968 Nonlinear two dimensional study flow with lift. J. Aircraft 5, pp. 135-143.

Herbst, W. B. 1980 Future fighter technologies. J. Aircraft 17, pp. 561-566.

Hitzel, S. M. and W. Schmidt 1984 Slender wings with leading edge vortex separation: A challenge for panel methods and Euler solvers. J. Aircraft 21, p. 751.

Hoeijmaker, H. W. M. and W. Vaatstra 1983 A higher order panel method applied to vortex sheet roll-up. AIAA J 21, pp. 516-523.

Hoerner, S. F. 1965 Fluid-Dynamic Drag p. 3-16. Brickburn, N. J.: Hoerner Fluid Dynamics.

Hoerner, S. F. 1975 Fluid-Dynamic Lift p. 17-6. Brickburn, N. J.: Hoerner Fluid Dynamics.

Polhamus, E. C. 1971 Predictions of vortex-lift characteristics by a leading-edge suction analogy. J. Aircraft 8, pp. 193-199.

Raj, P. and Rubin P. Gray 1978 Computation of two-dimensional potential flow wing elementary vortex distributions, J. Aircraft 15, pp. 698-700.

Poseidon Research Report No. 81

Rizzi, A and L. E. Eriksson 1984 Computation of flow around wings based on the Euler equation. JFM 148, pp. 45-71.

St Cyr, G. 1980 "A Computer Code for the Calculation of Aircraft Trailing Vortices," presented at Second International Symposium on Innovative Methods in Applied Engineering Science, Ecole Polytechnique de Montreal, Montreal, Canada, 16-20 June 1980.

Appendix A

Derivations of Force and Moment Theorems

The two-dimensional force and moment equations, (2.14) and (2.15), are simple enough to derive in Cartesian component notation. The corresponding derivations in three dimensions require the use of index notation.

a. Two Dimensions

In two dimensions, the vorticity equation (2.11) becomes

$$\frac{\partial \omega}{\partial t} + \underline{u} \cdot \nabla \omega = \frac{\partial g_y}{\partial x} - \frac{\partial g_x}{\partial y}, \quad (A1)$$

since the "vortex stretching" term $\underline{\omega} \cdot \nabla u$ is zero because of the absence of gradients in the z-direction.

Multiply by x and integrate over x and y :

$$\begin{aligned} \frac{d}{dt} \int_A x \omega \, dA + \int_A \left(x u \frac{\partial \omega}{\partial x} + x v \frac{\partial \omega}{\partial y} \right) dA \\ = \int_A \left(x \frac{\partial g_y}{\partial x} - x \frac{\partial g_x}{\partial y} \right) dA \end{aligned}$$

The r.h.s. can be rewritten and integrated to the (distant) boundary of A:

$$\begin{aligned} & \int_A \left\{ \frac{\partial}{\partial x} (xg_y) - g_y - \frac{\partial}{\partial y} (xg_x) \right\} dA \\ &= - \int_A g_y dA + \int_C (xg_y \hat{n}_x - xg_x \hat{n}_y) dC, \end{aligned}$$

Where n is the unit outward normal from the boundary C . The second term on the left can be reworked in a similar fashion:

$$\begin{aligned} & \int_A \left\{ \frac{\partial}{\partial x} (xu\omega) - x\omega \frac{\partial u}{\partial x} - u\omega - \frac{\partial}{\partial y} (xv\omega) - x\omega \frac{\partial v}{\partial y} \right\} dA \\ &= - \int_A u\omega dA + \int_C (xu\omega \hat{n}_x - xv\omega \hat{n}_y) dC, \end{aligned}$$

where use has been made of the continuity equation $\partial u/\partial x + \partial v/\partial y = 0$.

The perimeter C can be made large enough so that g and ω are both zero on it (ω is only affected by the fluid; it does not propagate instantaneously like a potential or even fast like a sound wave). The line integrals are then zero, and we have

$$- \int_A g_y dA = \frac{d}{dt} \int_A x\omega dA - \int_A u\omega dA.$$

But $\omega = \partial v / \partial x - \partial u / \partial y$, so the second term on the r.h.s. becomes

$$\begin{aligned} & \int_A \left\{ \frac{\partial}{\partial x} (uv) - v \frac{\partial u}{\partial x} - u \frac{\partial u}{\partial y} \right\} dA \\ &= \int_A \left\{ \frac{\partial}{\partial x} (uv) + v \frac{\partial v}{\partial y} - u \frac{\partial u}{\partial y} \right\} dA \\ &= \int_C \left\{ uv \hat{n}_x + (v^2 - u^2) \hat{n}_y / 2 \right\} dC . \end{aligned}$$

Since u and v fall to zero at least as fast as r^{-1} , the contour integral is again zero.

We finally have

$$- \int_A g_y dA = \frac{d}{dt} \int_A x \omega dA ,$$

from which

$$F_y = - \rho \int_A g_y dA = \rho \frac{d}{dt} \int_A x \omega dA .$$

This proves the y-component of (2.14). Proof of the x-component involves multiplying (A1) by y and proceeding as before.

The definition of moment per unit length in two-dimensional flow follows from (2.6):

$$M\hat{e}_z = - \int_A (xf_y - yf_x)\hat{e}_z dA . \quad (A2)$$

To prove the moment relation (2.15), we multiply (A1) by $r^2 = x^2 + y^2$ and proceed as before:

$$\begin{aligned} \frac{d}{dt} \int_A r^2 \omega dA + \int_A \left(r^2 u \frac{\partial \omega}{\partial x} + r^2 v \frac{\partial \omega}{\partial y} \right) dA \\ = \int_A \left(r^2 \frac{\partial g_y}{\partial x} - r^2 \frac{\partial g_x}{\partial y} \right) dA . \end{aligned} \quad (A3)$$

Dropping contour integrals as they come, we find for the r.h.s. that

$$\begin{aligned} \int_A \left\{ \frac{\partial}{\partial x} (r^2 g_y) - 2xg_y - \frac{\partial}{\partial y} (r^2 g_x) - 2yg_x \right\} dA \\ = - 2 \int_A (xg_y - yg_x) dA . \end{aligned} \quad (A4)$$

The second term on the left becomes

$$\begin{aligned}
 & \int_A \frac{\partial}{\partial x}(r^2 u \omega) + \frac{\partial}{\partial y}(r^2 v \omega) - r^2 \omega \left(\frac{\partial u}{\partial x} + \frac{\partial v}{\partial y} \right) - 2xu\omega - 2yv\omega \, dA \\
 &= -2 \int_A (xu\omega + yv\omega) \, dA \\
 &= -2 \int_A \left\{ xu \frac{\partial v}{\partial x} - xu \frac{\partial u}{\partial y} + yv \frac{\partial v}{\partial x} - yv \frac{\partial u}{\partial y} \right\} dA \\
 &= -2 \int_A \left\{ \frac{\partial}{\partial x}(xuv) - uv - xv \frac{\partial u}{\partial x} - \frac{\partial}{\partial y} \left(\frac{x^2}{2} \right) \right. \\
 &\quad \left. - \frac{\partial}{\partial y}(yuv) + uv - yu \frac{\partial v}{\partial y} + \frac{\partial}{\partial x} \left(\frac{y^2}{2} \right) \right\} dA \\
 &= -2 \int_A \left\{ xv \frac{\partial v}{\partial y} + yu \frac{\partial u}{\partial x} \right\} dA \\
 &= -2 \int_A \left\{ \frac{\partial}{\partial y} \frac{v^2}{2} + \frac{\partial}{\partial x} \left(\frac{u^2}{2} \right) \right\} dA \\
 &= 0 .
 \end{aligned}
 \tag{A5}$$

We have repeatedly made use of the assumption that quantities like xv^2 , yu^2 , etc. fall to zero faster than r^{-1} . That is so by virtue of (2.20), which implies that velocity falls as r^{-2} far from the region occupied by vorticity.

Combining (A2)-(A5), we obtain

$$M = \frac{\rho}{2} \frac{d}{dt} \int_A r^2 \omega \, dA ,$$

which is the same as (2.15).

b. Three Dimensions

The proofs of the two-dimensional force and moment theorems are fairly complicated. Matters get out of hand in three dimensions unless index notation is used. With index notation, the i th components of velocity and vorticity are represented as u_i and ω_i respectively. The curl involves the permutation symbol ϵ_{ijk} , so that

$$\omega_i = \epsilon_{ijk} \frac{\partial u_k}{\partial x_j} . \quad (A6)$$

ϵ_{ijk} is +1 if ijk are an even permutation of 123, -1 if ijk are an odd permutation of 123, and zero if two of the indices are the same. Another symbol of great utility is the Kronecker delta δ_{ij} , which is +1 if i and j are equal and zero if not. The continuity equation can thus be written as

$$\delta_{ij} \frac{\partial u_i}{\partial x_j} = 0 . \quad (A7)$$

Poseidon Research Report No. 81

Whenever indices are repeated, as in (A6) and (A7), they are summed over 1, 2, 3 (the Einstein summation convention).

ϵ and δ are connected by the identity

$$\epsilon_{ijk} \epsilon_{lmn} = \delta_{jm} \delta_{kn} - \delta_{km} \delta_{jn} , \quad (A8)$$

used frequently in the following proofs. Often we must rearrange the indices of ϵ to apply (A8). From the definition of ϵ ,

$$\epsilon_{ikj} = -\epsilon_{ijk} , \quad \epsilon_{kij} = \epsilon_{ijk} . \quad (A9)$$

Odd and even permutations of ϵ 's indices, exemplified by (A6), are used in the following without comment.

In index notation, the three-dimensional force theorem (2.14) becomes

$$\begin{aligned} F_i &= - \rho \int_V g_i dV \\ &= - \frac{\rho}{2} \frac{d}{dt} \int_V \epsilon_{ijk} x_j \omega_k dV , \end{aligned} \quad (A10)$$

where the first equality follows from the definition (2.5) of \underline{F} (with $\underline{f} = \rho \underline{g}$), and the second is to be proved.

The proof is based on the vorticity equation (2.11), which becomes

$$\frac{\partial \omega_k}{\partial t} + u_m \frac{\partial \omega_k}{\partial x_m} - \omega_m \frac{\partial u_k}{\partial x_m} = \epsilon_{kmn} \frac{\partial g_n}{\partial x_m}$$

in index notation. Take the cross-product with \underline{x} :

$$\epsilon_{ijk} x_j \frac{\partial \omega_k}{\partial t} + \epsilon_{ijk} x_j \left(u_m \frac{\partial \omega_k}{\partial x_m} - \omega_m \frac{\partial u_k}{\partial x_m} \right) = \epsilon_{ijk} \epsilon_{kmn} x_j \frac{\partial g_n}{\partial x_m} \quad (A11)$$

Apply the ϵ - δ identity to the r.h.s.:

$$\begin{aligned} \epsilon_{kij} \epsilon_{kmn} x_j \frac{\partial g_n}{\partial x_m} &= (\delta_{im} \delta_{jn} - \delta_{jn} \delta_{im}) x_j \frac{\partial g_n}{\partial x_m} \\ &= x_j \frac{\partial g_j}{\partial x_i} - x_j \frac{\partial g_i}{\partial x_j} \\ &= \frac{\partial}{\partial x_i} (x_j g_j) - g_j \delta_{ji} - \frac{\partial}{\partial x_j} (x_j g_i) + g_i \delta_{jj} \\ &= \frac{\partial}{\partial x_i} (x_j g_i) - \frac{\partial}{\partial x_j} (x_j g_i) + 2g_i \quad , \quad (A12) \end{aligned}$$

where we have used the facts that $\partial x_j / \partial x_i = \delta_{ji}$ and $\delta_{jj} = 1 + 1 + \dots = 3$. Rework the second term on the l.h.s. in like fashion:

$$\begin{aligned}
 & \epsilon_{ijk} x_j \left(u_m \frac{\partial \omega_k}{\partial x_m} - \omega_m \frac{\partial u_k}{\partial x_m} \right) \\
 &= \epsilon_{ijk} \left\{ \frac{\partial}{\partial x_m} (x_j u_m \omega_k) - u_m \omega_k \delta_{jm} \right. \\
 &\quad \left. - \frac{\partial}{\partial x_m} (x_j \omega_m u_k) - \omega_m u_k \delta_{jm} \right\} \\
 &= \frac{\partial}{\partial x_m} \left\{ \epsilon_{ijk} x_j (u_m \omega_k - \omega_m u_k) \right\} - 2 \epsilon_{ijk} u_j \omega_k. \quad (A13)
 \end{aligned}$$

Moreover,

$$\begin{aligned}
 \epsilon_{ijk} u_j \omega_k &= \epsilon_{ijk} \epsilon_{kmn} u_j \frac{\partial u_n}{\partial x_m} \\
 &= (\delta_{im} \delta_{jn} - \delta_{jm} \delta_{in}) u_j \frac{\partial u_n}{\partial x_m} \\
 &= u_j \frac{\partial u_j}{\partial x_i} - u_j \frac{\partial u_i}{\partial x_j} = \frac{\partial}{\partial x_i} \frac{u_j u_j}{2} - \frac{\partial}{\partial x_j} (u_i u_j) \quad (A14)
 \end{aligned}$$

Gathering (A11)-(A14), integrating over an arbitrarily large volume V , and eliminating surface integrals involving ω_i or g_i , we obtain

$$2 \int_V g_i dV = \frac{d}{dt} \int_V \epsilon_{ijk} x_j \omega_k dV$$

$$- 2 \int_S \frac{u_j u_j}{2} \hat{n}_i - u_i u_j \hat{n}_j dS .$$

Velocity components u_i fall at least as fast as r^{-2} in three dimensions, so the surface integral vanishes, and we have proved (A10).

The definition of moment (2.6) and the moment theorem (2.17) require us to prove that

$$\int_V \epsilon_{ijk} x_j g_k dV = \frac{1}{3} \frac{d}{dt} \int_V \epsilon_{ijk} x_j (\epsilon_{kmn} x_m \omega_n) dV \quad (A15)$$

The proof is complicated and will only be sketched here. Cross the vorticity equation twice with \underline{x} :

$$\epsilon_{ijk} x_j \epsilon_{kmn} x_m \frac{\partial \omega_n}{\partial t} + \epsilon_{ijk} x_j \epsilon_{kmn} x_m \left(u_p \frac{\partial \omega_n}{\partial x_p} - \omega_p \frac{\partial u_n}{\partial x_p} \right)$$

$$= \epsilon_{ijk} x_j \epsilon_{kmn} x_m \epsilon_{npq} \frac{\partial g_q}{\partial x_p} . \quad (A16)$$

Manipulate the r.h.s.:

$$\begin{aligned}
 & \epsilon_{ijk} x_j \left(\epsilon_{nkm} \epsilon_{npq} x_m \frac{\partial g_q}{\partial x_p} \right) \\
 &= \epsilon_{ijk} x_j (\delta_{kp} \delta_{mq} - \delta_{mp} \delta_{kq}) x_m \frac{\partial g_q}{\partial x_p} \\
 &= \epsilon_{ijk} x_j \left(x_m \frac{\partial g_m}{\partial x_k} - x_m \frac{\partial g_q}{\partial x_p} \right) \\
 &= \epsilon_{ijk} \left\{ \frac{\partial}{\partial x_k} (x_j x_m g_m) - x_j g_m \delta_{km} - x_m g_m \delta_{kj} \right. \\
 &\quad \left. - \frac{\partial}{\partial x_k} (x_j x_m g_k) + x_j g_k \delta_{mm} + x_m g_k \delta_{mj} \right\} \\
 &= \epsilon_{ijk} \left\{ \frac{\partial}{\partial x_k} (x_j x_m g_m) - \frac{\partial}{\partial x_m} (x_j x_m g_k) \right. \\
 &\quad \left. - x_j g_k + 3x_j g_k + x_j g_k \right\}
 \end{aligned}$$

The second term on the left of (A16) can be written entirely in terms of divergences. Integrating (A15) over all space, we find that

$$\begin{aligned} \frac{d}{dt} \int_V \epsilon_{ijk} x_j \epsilon_{kmn} x_m \omega_n dV \\ = 3 \int_V \epsilon_{ijk} x_j g_k dV , \end{aligned}$$

where the surface integrals vanish provided that ω_i and g_i are confined to a finite domain, and that $x_j u_m u_n$ falls to zero faster than r^{-2} , which is always true. This confirms (A15) and hence (2.17).

Appendix B

Bound Vorticity on a Flat Plate at Angle of Attack
in Potential Flow

Bound vorticity must exactly cancel the normal component of freestream velocity; that is,

$$U \sin \alpha = \int_0^c \frac{\gamma(x') dx'}{2\pi(x-x')} \text{ for } 0 \leq x \leq c .$$

Apply the Glauert transformation

$$x' = \frac{c}{2}(1 - \cos \theta') ,$$

so that

$$U \sin \alpha = \frac{1}{2\pi} \int_0^{2\pi} \frac{\gamma(\theta') \sin \theta' d\theta'}{\cos \theta' - \cos \theta} .$$

Use the fact that

$$\int_0^{\pi} \frac{\cos n\theta' d\theta'}{\cos \theta' - \cos \theta} = \frac{\pi \sin n\theta}{\sin \theta}$$

to guess that

Poseidon Research Report No. 81

$$\gamma(\theta') \sin \theta' = A_0 + B \cos \theta' .$$

A_0 must be zero to satisfy the circulation theorem. Then

$$U \sin \alpha = B_0/2 .$$

Thus

$$\gamma = 2 U \sin \alpha \tanh \theta = U \sin \frac{1 - 2x/C}{\sqrt{(x/c)[1-(x/c)]}} .$$

DATE
FILMED
-8